Journal of Computational Physics 403 (2020) 109072

Contents lists available at ScienceDirect

Journal of Computational Physics

www.elsevier.com/locate/jcp

A free–energy stable nodal discontinuous Galerkin approximation with summation–by–parts property for the Cahn–Hilliard equation

Juan Manzanero [a,b,*], Gonzalo Rubio [a,b], David A. Kopriva [c], Esteban Ferrer [a,b], Eusebio Valero [a,b]

[a] ETSIAE-UPM - School of Aeronautics, Universidad Politécnica de Madrid, Plaza Cardenal Cisneros 3, E-28040 Madrid, Spain
[b] Center for Computational Simulation, Universidad Politécnica de Madrid, Campus de Montegancedo, Boadilla del Monte, 28660, Madrid, Spain
[c] Department of Mathematics, Florida State University and Computational Science Research Center, San Diego State University, United States of America

ARTICLE INFO

Article history:
Received 27 February 2019
Received in revised form 13 September 2019
Accepted 27 October 2019
Available online 31 October 2019

Keywords:
Cahn–Hilliard
Summation–by–parts property
High-order methods
Discontinuous Galerkin

ABSTRACT

We present a nodal Discontinuous Galerkin (DG) scheme for the Cahn–Hilliard equation that satisfies the summation–by–parts simultaneous–approximation–term (SBP–SAT) property. The latter permits us to show that the discrete free–energy is bounded, and as a result, the scheme is provably stable. The scheme and the stability proof are presented for general curvilinear three–dimensional hexahedral meshes. We use the Bassi–Rebay 1 (BR1) scheme to compute interface fluxes, and a first order IMplicit–EXplicit (IMEX) scheme to integrate in time. We provide a semi–discrete stability study, and a fully–discrete proof subject to a positivity condition on the solution. Lastly, we test the theoretical findings using numerical cases that include two and three–dimensional problems.

1. Introduction

Phase field models describe the phase separation dynamics of two immiscible liquids by minimizing a chosen free–energy. For an arbitrary free–energy function, it is possible to construct different phase field models. Amongst the most popular, one can find the Cahn–Hilliard [1] and the Allen–Cahn [2] models. The popularity of the first, despite being a fourth order operator in space, comes from its ability to conserve phases [3].

In this paper we present a nodal Discontinuous Galerkin (DG) spectral element method (DGSEM) for the Cahn–Hilliard equation [1]. In particular, this work uses the Gauss–Lobatto version of the DGSEM, which makes it possible to obtain energy–stable schemes using the summation–by–parts simultaneous–aproximation–term (SBP–SAT) property. Moreover, it handles arbitrary three dimensional curvilinear hexahedral meshes whilst maintaining high-order spectral accuracy and free–energy stability. An alternative, which is not considered in this work, but has been studied in [4], is to use consistent integration in all quadratures used in the weak–formulation.

The summation–by–parts simultaneous–approximation–term (SBP–SAT) property originates with finite difference methods [5–7], and also allows one to construct discontinuous Galerkin schemes that are provably stable [8,9]. Different authors

* Corresponding author.
E-mail address: juan.manzanero@upm.es (J. Manzanero).

https://doi.org/10.1016/j.jcp.2019.109072
0021-9991/

have presented energy– and entropy–stable discontinuous Galerkin schemes using this framework for the linear advection equation [10,11], Burgers equation [12,13], shallow water equations [14], Euler and Navier–Stokes equations [15,13,16], and the magneto–hydrodynamics equations [17], among others.

Following these ideas, we present a free–energy stable approximation for the Cahn–Hilliard equation. The stability analysis presented here is both semi–discrete (assuming exact integration in time) and fully–discrete (i.e. considering the discrete approximation of space and time). Since the Cahn–Hilliard equation is fourth order in space, the numerical stiffness of the scheme leads to impractical time step limitations when using explicit methods. Therefore, we study the stability of a first order IMplicit–EXplicit (IMEX) approximation in time, which has been previously used for the Cahn–Hilliard equation [18], and whose efficiency is similar to that of explicit methods. This is possible since the scheme is designed to have a constant (in time) coefficient matrix of the linear system. Without loss of generality, we use LU factorization and Gauss elimination, but iterative solvers could be used.

The rest of this paper is organized as follows: In Sec. 2, we introduce the Cahn–Hilliard equation and derive a continuous energy estimate. Next, in Sec. 3, we construct the DG approximation. In Sec. 4, we perform the energy analysis in a semi–discrete fashion in Sec. 4.1 and fully–discrete in Sec. 4.2. Lastly, we provide numerical experiments in Sec. 5 that assess the capabilities of the method.

2. Cahn–Hilliard equation and continuous energy estimates

In this section we give a brief description of the Cahn–Hilliard equation and its properties. Amongst the different Cahn–Hilliard settings, we solve the constant mobility model, with polynomic double–well chemical free–energy, and we restrict ourselves to two–phase flows [19,20]. The Cahn–Hilliard equation describes the phase separation dynamics of binary alloys or two phase flows. The phase field variable, ϕ, satisfies the evolution equation

$$\phi_t = \nabla \cdot (M \nabla w), \quad \text{in } \Omega, \tag{1}$$

where M is a positive parameter named mobility, Ω is the physical domain (with boundaries $\partial\Omega$), and w is a scalar field called the *chemical potential*. The chemical energy is designed to minimize an arbitrary free–energy functional, $\mathcal{F}(\phi, \nabla\phi)$, which depends on the phase field and its gradients,

$$w = \frac{\delta \mathcal{F}}{\delta \phi}. \tag{2}$$

For the chemical potential, w, we apply a homogeneous Neumann boundary condition to guarantee mass conservation,

$$\nabla w \cdot \vec{n}\Big|_{\partial\Omega} = 0. \tag{3}$$

The free–energy is constructed so that two opposing effects balance: the chemical free–energy, ψ, which favors phase separation, and the interfacial energy $\frac{1}{2}k|\nabla\phi|^2$, which favors homogenization,

$$\mathcal{F} = \int_\Omega \left(\psi(\phi) + \frac{1}{2} k |\nabla \phi|^2 \right) \mathrm{d}\vec{x} - \int_{\partial\Omega} g(\phi)\, \mathrm{d}S = F_v(\phi) + F_s(\phi). \tag{4}$$

In (4) we have introduced $F_v(\phi)$ and $F_s(\phi)$ as the volumetric and surface free–energies respectively, where $g(\phi)$ represents a boundary energy that will also be minimized with appropriate boundary conditions, and k is the interfacial energy coefficient.

To perform the minimization, one linearizes the free–energy (4) around an equilibrium solution,

$$\delta\mathcal{F} = \int_\Omega \left(\frac{\mathrm{d}\psi}{\mathrm{d}\phi}\delta\phi + k\nabla\phi \cdot \nabla(\delta\phi) \right) \mathrm{d}\vec{x} - \int_{\partial\Omega} \frac{\mathrm{d}g}{\mathrm{d}\phi}\delta\phi\, \mathrm{d}S, \tag{5}$$

where $\delta\phi$ is a small perturbation. Since we will also apply Neumann boundary conditions for ϕ, the perturbation $\delta\phi$ is not restricted to vanish at the boundaries $\partial\Omega$. We integrate the second term of the first integral in (5) by parts,

$$\delta\mathcal{F} = \int_\Omega \left(\frac{\mathrm{d}\psi}{\mathrm{d}\phi} - k\nabla^2\phi \right) \delta\phi\, \mathrm{d}\vec{x} - \int_{\partial\Omega} \left(\frac{\mathrm{d}g}{\mathrm{d}\phi} - k\nabla\phi\cdot\vec{n} \right) \delta\phi\, \mathrm{d}S, \tag{6}$$

which yields both the chemical potential definition

$$w = \frac{\mathrm{d}\psi}{\mathrm{d}\phi} - k\nabla^2\phi, \tag{7}$$

and the appropriate Neumann boundary conditions prescription

$$k\nabla\phi\cdot\vec{n}\Big|_{\partial\Omega}=\frac{\mathrm{d}g}{\mathrm{d}\phi}. \tag{8}$$

In this work we use the polynomial double–well function for the chemical free–energy [1],

$$\psi(\phi)=\frac{1}{4}(1-\phi)^2(1+\phi)^2, \tag{9}$$

and a linear function for the boundary energy,

$$g(\phi)=\beta\phi, \tag{10}$$

since they represent standard choices in the literature, but other choices that are not covered here exist (e.g. logarithmic chemical free–energy [21]).

2.1. Continuous free–energy stability bound

We first show that the free–energy is bounded by that computed with a given initial condition. To do so, we follow [4] and transform the fourth order equation into a system of four first order equations. As a result, we construct four weak forms

$$\langle\phi_t,\varphi_\phi\rangle=\left\langle\nabla\cdot\left(M\vec{f}\right),\varphi_\phi\right\rangle, \tag{11a}$$

$$\left\langle\vec{f},\vec{\varphi}_f\right\rangle=\langle\nabla w,\vec{\varphi}_f\rangle, \tag{11b}$$

$$\langle w,\varphi_w\rangle=\left\langle\frac{\mathrm{d}\psi}{\mathrm{d}\phi},\varphi_w\right\rangle-k\langle\nabla\cdot\vec{q},\varphi_w\rangle, \tag{11c}$$

$$\langle\vec{q},\vec{\varphi}_q\rangle=\langle\nabla\phi,\vec{\varphi}_q\rangle, \tag{11d}$$

where we introduced the auxiliary variables $\vec{q}=\nabla\phi$ and $\vec{f}=\nabla w$, two arbitrary L^2 scalar test functions φ_ϕ and φ_w, and their two vectorial counterparts $\vec{\varphi}_f$ and $\vec{\varphi}_q$. The operator $\langle f,g\rangle$ is the L^2 inner product

$$\langle f,g\rangle=\int_\Omega fg\,\mathrm{d}\vec{x}, \tag{12}$$

which induces the L^2 norm,

$$\langle f,f\rangle=\int_\Omega f^2\,\mathrm{d}\vec{x}=||f||^2. \tag{13}$$

We integrate (11a) and (11c) by parts,

$$\begin{aligned}\langle\phi_t,\varphi_\phi\rangle&=\int_{\partial\Omega}M\vec{f}\cdot\vec{n}\varphi_\phi\,\mathrm{d}S-\left\langle M\vec{f},\nabla\varphi_\phi\right\rangle,\\ \langle w,\varphi_w\rangle&=\left\langle\frac{\mathrm{d}\psi}{\mathrm{d}\phi},\varphi_w\right\rangle-k\int_{\partial\Omega}\vec{q}\cdot\vec{n}\varphi_w\,\mathrm{d}S+k\langle\vec{q},\nabla\varphi_w\rangle,\end{aligned} \tag{14}$$

and apply the boundary conditions (8) and (3) to (14),

$$\langle\phi_t,\varphi_\phi\rangle=-\left\langle M\vec{f},\nabla\varphi_\phi\right\rangle, \tag{15a}$$

$$\langle w,\varphi_w\rangle=\left\langle\frac{\mathrm{d}\psi}{\mathrm{d}\phi},\varphi_w\right\rangle-k\int_{\partial\Omega}\frac{\mathrm{d}g}{\mathrm{d}\phi}\varphi_w\,\mathrm{d}S+k\langle\vec{q},\nabla\varphi_w\rangle. \tag{15b}$$

Next, we set $\varphi_\phi = w$ in (15a),

$$\langle \phi_t, w \rangle = -\left\langle M\vec{f}, \nabla w \right\rangle = -\left\langle M\vec{f}, \vec{f} \right\rangle \leqslant 0, \tag{16}$$

where we used (11b) in the last equality. Similarly, we let $\varphi_w = \mathrm{d}\phi/\mathrm{d}t = \phi_t$ in (15b),

$$\langle w, \phi_t \rangle = \left\langle \frac{\mathrm{d}\psi}{\mathrm{d}\phi}, \phi_t \right\rangle + k\langle \vec{q}, \nabla\phi_t \rangle - \int_{\partial\Omega} \frac{\mathrm{d}g}{\mathrm{d}\phi}\phi_t \,\mathrm{d}S. \tag{17}$$

Lastly, we use the chain rule in time for each of the three terms in (17),

$$\begin{aligned}
&\left\langle \frac{\mathrm{d}\psi}{\mathrm{d}\phi}, \phi_t \right\rangle = \int_\Omega \frac{\mathrm{d}\psi}{\mathrm{d}\phi}\phi_t \,\mathrm{d}\Omega = \frac{\mathrm{d}}{\mathrm{d}t}\int_\Omega \psi \,\mathrm{d}\Omega, \\
&k\langle \vec{q}, \nabla\phi_t \rangle = k\langle \vec{q}, \vec{q}_t \rangle = k\int_\Omega \vec{q}\cdot\vec{q}_t \,\mathrm{d}\Omega = \frac{k}{2}\frac{\mathrm{d}}{\mathrm{d}t}\int_\Omega |\vec{q}|^2 \,\mathrm{d}\Omega, \\
&\int_{\partial\Omega} \frac{\mathrm{d}g}{\mathrm{d}\phi}\phi_t \,\mathrm{d}S = \frac{\mathrm{d}}{\mathrm{d}t}\int_{\partial\Omega} g(\phi)\,\mathrm{d}S,
\end{aligned} \tag{18}$$

which when replaced in (17) yields the time derivative of the free–energy $\mathcal{F}$,

$$\langle w, \phi_t \rangle = \frac{\mathrm{d}}{\mathrm{d}t}\int_\Omega \left(\psi + \frac{k}{2}|\vec{q}|^2\right)\mathrm{d}\Omega - \frac{\mathrm{d}}{\mathrm{d}t}\int_{\partial\Omega} g(\phi)\,\mathrm{d}S = \frac{\mathrm{d}\mathcal{F}}{\mathrm{d}t}. \tag{19}$$

Therefore, by substituting $\langle w, \phi_t \rangle$ from (19) into (16) we find the bound for the free–energy time derivative,

$$\frac{\mathrm{d}\mathcal{F}}{\mathrm{d}t} = -\left\langle M\vec{f}, \vec{f} \right\rangle \leqslant 0, \tag{20}$$

which we can integrate in time to show that

$$\mathcal{F}(T) = \mathcal{F}(0) - \int_0^T \left\langle M\vec{f}, \vec{f} \right\rangle dt \leqslant \mathcal{F}(0). \tag{21}$$

As a result, the Cahn–Hilliard equation (1) with chemical potential (7) and Neumann boundary conditions (3) and (8) guarantees that the free–energy $\mathcal{F}$, defined in (4), is bounded in time, and is the property to be mimicked by the subsequent approximation.

3. The nodal discontinuous Galerkin spectral element method

In this section we describe the construction of the nodal Discontinuous Galerkin Spectral Element Method (DGSEM). From all the variants, we restrict ourselves to the tensor product DGSEM with Gauss–Lobatto (GL) points (DGSEM–GL), since it satisfies the summation–by–parts simultaneous–approximation–term (SBP–SAT) property. The latter is used to prove the scheme's stability without relying on exact integration.

The computational domain Ω is tessellated with non–overlapping hexahedral elements, which are then geometrically transformed to a reference element $E = [-1, 1]^3$ by means of a polynomial mapping that relates physical ($\vec{x} = (x^1, x^2, x^3) = (x, y, z)$) and local ($\vec{\xi} = (\xi^1, \xi^2, \xi^3) = (\xi, \eta, \zeta)$) coordinates through

$$\vec{x} = \vec{X}(\vec{\xi}) = \vec{X}(\xi, \eta, \zeta). \tag{22}$$

Let $\vec{S}_{L/R}(\eta, \zeta)$, $\vec{S}_{F/Ba}(\xi, \zeta)$, and $\vec{S}_{T/Bo}(\xi, \eta)$ be order N tensor product polynomial approximations of the (curvilinear) left, right, front, back, top, and bottom faces respectively of an element. We construct the transfinite mapping with a linear interpolation between those,

$$
\begin{aligned}
\vec{X} = \quad & \frac{1}{2}\vec{S}_L(\eta,\zeta)(1-\xi) + \frac{1}{2}\vec{S}_R(\eta,\zeta)(\xi+1) + \frac{1}{2}\vec{S}_F(\xi,\zeta)(1-\eta) + \frac{1}{2}\vec{S}_{Ba}(\xi,\zeta)(\eta+1) \\
& + \frac{1}{2}\vec{S}_{Bo}(\xi,\eta)(1-\zeta) + \frac{1}{2}\vec{S}_T(\xi,\eta)(\zeta+1) - \frac{1}{4}\vec{S}_{Bo}(\xi,-1)(1-\eta)(1-\zeta) \\
& - \frac{1}{4}\vec{S}_{Bo}(1,\eta)(1+\xi)(1-\zeta) - \frac{1}{4}\vec{S}_{Bo}(\xi,1)(\eta+1)(1-\zeta) - \frac{1}{4}\vec{S}_{Bo}(-1,\eta)(1-\xi)(1-\zeta) \\
& - \frac{1}{4}\vec{S}_T(\xi,-1)(1-\eta)(1+\zeta) - \frac{1}{4}\vec{S}_T(1,\eta)(1+\xi)(1+\zeta) - \frac{1}{4}\vec{S}_T(\xi,1)(\eta+1)(1+\zeta) \\
& - \frac{1}{4}\vec{S}_T(-1,\eta)(1-\xi)(1+\zeta) - \frac{1}{4}\vec{S}_L(-1,\zeta)(1-\xi)(1-\eta) - \frac{1}{4}\vec{S}_L(1,\zeta)(1-\xi)(1+\eta) \\
& - \frac{1}{4}\vec{S}_R(-1,\zeta)(1+\xi)(1-\eta) - \frac{1}{4}\vec{S}_R(1,\zeta)(1+\xi)(1+\eta) \\
& + \frac{1}{8}\vec{S}_{Bo}(-1,-1)(1-\xi)(1-\eta)(1-\zeta) + \frac{1}{8}\vec{S}_{Bo}(1,-1)(1+\xi)(1-\eta)(1-\zeta) \\
& + \frac{1}{8}\vec{S}_{Bo}(-1,1)(1-\xi)(1+\eta)(1-\zeta) + \frac{1}{8}\vec{S}_{Bo}(1,1)(1+\xi)(1+\eta)(1-\zeta) \\
& + \frac{1}{8}\vec{S}_T(-1,-1)(1-\xi)(1-\eta)(1+\zeta) + \frac{1}{8}\vec{S}_T(1,-1)(1+\xi)(1-\eta)(1+\zeta) \\
& + \frac{1}{8}\vec{S}_T(-1,1)(1-\xi)(1+\eta)(1+\zeta) + \frac{1}{8}\vec{S}_T(1,1)(1+\xi)(1+\eta)(1+\zeta).
\end{aligned}
\tag{23}
$$

We use polynomial interpolants of order N to approximate the solutions inside an element E. These polynomials are written as tensor products of the Lagrange interpolating polynomials, $l_j(\xi)$,

$$
l_j(\xi) = \prod_{\substack{i=0 \\ i\neq j}}^{N} \frac{\xi - \xi_i}{\xi_j - \xi_i}, \quad j = 0, \ldots, N, \tag{24}
$$

whose nodes are a set of Gauss–Lobatto points $\{\xi_i\}_{i=0}^N$, $\{\eta_i\}_{i=0}^N$, and $\{\zeta_i\}_{i=0}^N$ in the reference element E. The polynomial interpolant of a function u in E is therefore

$$
\mathcal{I}^N[u(x,y,z,t)]_E = U(\xi,\eta,\zeta,t) = \sum_{i,j,k=0}^{N} U_{ijk}(t) l_i(\xi) l_j(\eta) l_k(\zeta). \tag{25}
$$

In (25), $U_{ijk}(t)$ represents the (time dependent) nodal values of an arbitrary function u. Note that we use lower cases for functions, whilst upper cases represent a polynomial interpolant.

The Lagrange polynomials satisfy by construction the cardinal property

$$
l_j(\xi_i) = \delta_{ij}, \tag{26}
$$

where δ_{ij} is the Kronecker delta. To approximate integrals, we use a quadrature rule using GL nodes and weights $\{w_j\}_{j=0}^N$ which provides a precision of order $2N-1$ (see [22]),

$$
\int_{-1}^{1} FG \,\mathrm{d}\xi \approx \int_{E,N} FG \,\mathrm{d}\xi = \sum_{m=0}^{N} w_m F_m G_m. \tag{27}
$$

The associated Lagrange polynomials are discretely orthogonal

$$
\int_{E,N} l_i(\xi) l_j(\xi) \,\mathrm{d}\xi = w_i \delta_{ij}, \tag{28}
$$

and the definition of the quadrature weights w_i for $i = j$ are

$$
w_i = \int_{E,N} l_i(\xi)^2 \,\mathrm{d}\xi = \int_{E,N} l_i(\xi) \,\mathrm{d}\xi = \int_{-1}^{1} l_i(\xi) \,\mathrm{d}\xi. \tag{29}
$$

Furthermore, we chose GL nodes since the quadrature rule (27) with weights (29) satisfies the discrete summation–by–parts simultaneous–approximation–term (SBP–SAT) property, that is, the integration by parts rule holds discretely, which in one dimension is

$$\int_{E,N} \frac{\mathrm{d}U}{\mathrm{d}\xi} V \,\mathrm{d}\xi = U_N V_N - U_0 V_0 - \int_{E,N} U \frac{\mathrm{d}V}{\mathrm{d}\xi} \,\mathrm{d}\xi. \tag{30}$$

The SBP–SAT property is used to follow the continuous analysis steps that prove the boundedness of the free energy $\mathcal{F}$ in (21) discretely.

To construct the integrals that define the discrete weak–formulation of (11) in a general curvilinear 3D configuration, we construct the covariant

$$\vec{a}_j = \frac{\partial \vec{X}}{\partial \xi^j}, \quad j = 1,2,3, \tag{31}$$

and contravariant

$$\vec{a}^j = \nabla \xi^j, \quad j = 1,2,3, \tag{32}$$

vector bases. The covariant and (volume weighted) contravariant bases are related by

$$J\vec{a}^i = \vec{a}_j \times \vec{a}_k, \quad (i,j,k) \text{ cyclic}, \tag{33}$$

where the Jacobian of the transformation is

$$J = \vec{a}_1 \cdot \left(\vec{a}_2 \times \vec{a}_3\right). \tag{34}$$

However, the continuous metric identities

$$\sum_{i=1}^{3} \frac{\partial J a_n^i}{\partial \xi^i} = 0, \quad n = 1,2,3, \tag{35}$$

do not hold discretely for (33), since the product $\vec{a}_i \times \vec{a}_j$ is a polynomial of order $2N$. Therefore, we construct the discrete contravariant basis in curl form

$$J a_n^i = -\hat{\vec{x}}^i \cdot \nabla_\xi \times \mathcal{I}^N \left(X_l \nabla_\xi X_m\right), \quad i,n = 1,2,3, \quad (n,m,l) \text{ cyclic}, \tag{36}$$

so that they satisfy the metric identities discretely [23]. In (36), $J a_n^i$ is the $n-$th Cartesian component of the contravariant vector $J\vec{a}^i$, $\hat{\vec{x}}^i$ is the $i-$th Cartesian unit vector, and $\nabla_\xi = (\partial/\partial\xi, \partial/\partial\eta, \partial/\partial\zeta)$.

We use the contravariant basis to transform differential operators from physical to computational space. The divergence of a vector is

$$\nabla \cdot \vec{F} = \frac{1}{J} \nabla_\xi \cdot \left(\boldsymbol{\mathcal{M}}^T \vec{F}\right) = \frac{1}{J} \nabla_\xi \cdot \tilde{\boldsymbol{F}}, \tag{37}$$

where,

$$\left[\tilde{F}^1 \ \tilde{F}^2 \ \tilde{F}^3\right]^T = \tilde{\boldsymbol{F}} = \boldsymbol{\mathcal{M}}^T \vec{F}, \tag{38}$$

is the contravariant flux, and

$$\boldsymbol{\mathcal{M}} = [J\vec{a}^1 \ \ J\vec{a}^2 \ \ J\vec{a}^3] = [J\vec{a}^\xi \ \ J\vec{a}^\eta \ \ J\vec{a}^\zeta], \tag{39}$$

is the Jacobian matrix of the transformation. The gradient of a scalar is

$$\nabla U = \frac{1}{J} \boldsymbol{\mathcal{M}} \nabla_\xi U. \tag{40}$$

Lastly, using the transformation Jacobian (34), we approximate the three dimensional integrals in an element using Gauss-Lobatto quadrature. Let $\mathcal{J}$ be the polynomial approximation of the mapping Jacobian (34) (using (25)), then the quadrature is,

$$\int_e F\, G \,\mathrm{d}e \approx \int_{E,N} \mathcal{J} F\, G \,\mathrm{d}E = \langle \mathcal{J}F, G \rangle_{E,N} = \sum_{i,j,k=0}^{N} w_{ijk} \mathcal{J}_{ijk} F_{ijk} G_{ijk}, \tag{41}$$

with associated norm $||F||^2_{J,N} = \langle \mathcal{J}F, F \rangle_{E,N}$. Eq. (41) allows us to write the discrete summation–by–parts property as in [8]

$$\left\langle \nabla_\xi U, \tilde{\boldsymbol{F}} \right\rangle_{E,N} = \int_{\partial E,N} U \tilde{\boldsymbol{F}} \cdot \hat{\boldsymbol{n}} \,\mathrm{d}S_\xi - \left\langle \nabla_\xi \cdot \tilde{\boldsymbol{F}}, U \right\rangle_{E,N}. \tag{42}$$

In (42), $\hat{\tilde{n}}$ is the reference space unit outward normal vector at the element faces, $\mathrm{d}S_\xi$ is the surface local integration variables ($\mathrm{d}S^i_\xi = \pm \mathrm{d}\xi^j\,\mathrm{d}\xi^k$ for i–oriented faces). To compute the surface integral, we write two dimensional quadratures in each of the six faces that define the element,

$$\int_{\partial E,N} U\tilde{\boldsymbol{F}}\cdot\hat{\boldsymbol{n}}\,\mathrm{d}S_\xi = \int_{f,N} U\tilde{F}^\xi\,\mathrm{d}\eta\,\mathrm{d}\zeta\Big|_{\xi=-1}^{\xi=1} + \int_{f,N} U\tilde{F}^\eta\,\mathrm{d}\xi\,\mathrm{d}\zeta\Big|_{\eta=-1}^{\eta=1} + \int_{f,N} U\tilde{F}^\zeta\,\mathrm{d}\xi\,\mathrm{d}\eta\Big|_{\zeta=-1}^{\zeta=1}. \tag{43}$$

Moreover, we can write surface integrals in either physical or computational space. The relation to the physical surface integration variables is

$$\mathrm{d}S^i = \left|J\vec{a}^i\right|\,\mathrm{d}\xi^j\,\mathrm{d}\xi^k = \mathcal{J}^i_f\,\mathrm{d}S^i_\xi, \tag{44}$$

where we defined the face Jacobian $\mathcal{J}^i_f = \left|\mathcal{J}\vec{a}^i\right|$. We can relate the surface flux in both reference element, $\tilde{\boldsymbol{F}}\cdot\hat{\boldsymbol{n}}$, and physical, $\vec{F}\cdot\vec{n}$, variables through

$$\tilde{\vec{F}}\cdot\hat{\vec{n}}^i\,\mathrm{d}S_\xi = \left(\boldsymbol{\mathcal{M}}^T\vec{F}\right)\cdot\hat{\vec{n}}^i\,\mathrm{d}S_\xi = \vec{F}\cdot\left(\boldsymbol{\mathcal{M}}\hat{\vec{n}}^i\right)\mathrm{d}S_\xi = \vec{F}\cdot\vec{n}\left|J\vec{a}^i\right|\,\mathrm{d}S_\xi = \vec{F}\cdot\vec{n}^i\,\mathrm{d}S. \tag{45}$$

Therefore, quadratures can be represented both in physical and computational spaces,

$$\int_{\partial E,N}\tilde{\vec{F}}\cdot\hat{\vec{n}}\,\mathrm{d}S_\xi = \int_{\partial e,N}\vec{F}\cdot\vec{n}\,\mathrm{d}S, \tag{46}$$

and we will use one or the other depending on whether we are studying an isolated element (computational space) or the whole combination of elements in the mesh (physical space).

3.1. Discontinuous Galerkin spectral element approximation of the Cahn–Hilliard equation

We now construct the discrete version of (11). We first transform (11) to the local coordinate system as described in (37) and (40), and construct four weak forms inside the reference element E. To do so, we restrict the test functions φ_Φ, φ_W (scalar), $\vec{\varphi}_{\tilde{F}}$, $\vec{\varphi}_{\tilde{Q}}$ (vectorial), to the order N polynomial space,

$$\langle J\phi_t,\varphi_\Phi\rangle_E = \left\langle\nabla_\xi\cdot\left(M\tilde{\boldsymbol{f}}\right),\varphi_\Phi\right\rangle_E, \tag{47a}$$

$$\left\langle J\vec{f},\vec{\varphi}_F\right\rangle_E = \langle\boldsymbol{\mathcal{M}}\nabla_\xi w,\vec{\varphi}_F\rangle_E = \left\langle\nabla_\xi w,\boldsymbol{\mathcal{M}}^T\vec{\varphi}_F\right\rangle_E = \langle\nabla_\xi w,\tilde{\boldsymbol{\varphi}}_F\rangle_E, \tag{47b}$$

$$\langle Jw,\varphi_W\rangle_E = \left\langle J\frac{\mathrm{d}\psi}{\mathrm{d}\phi},\varphi_W\right\rangle_E - k\langle\nabla_\xi\cdot\tilde{\boldsymbol{q}},\varphi_W\rangle_E, \tag{47c}$$

$$\left\langle J\vec{q},\vec{\varphi}_Q\right\rangle_E = \langle\boldsymbol{\mathcal{M}}\nabla_\xi\phi,\vec{\varphi}_Q\rangle_E = \left\langle\nabla_\xi\phi,\boldsymbol{\mathcal{M}}^T\vec{\varphi}_Q\right\rangle_E = \langle\nabla_\xi\phi,\tilde{\boldsymbol{\varphi}}_Q\rangle_E. \tag{47d}$$

Next, we integrate the right hand side terms that contain a ∇_ξ operator by parts, replace the continuous functions by their polynomial approximations, and replace exact integrals by quadratures,

$$\langle\mathcal{J}\Phi_t,\varphi_\Phi\rangle_{E,N} = \int_{\partial E,N}\varphi_\Phi\left(M\tilde{\boldsymbol{F}}\right)^\star\cdot\hat{\boldsymbol{n}}\,\mathrm{d}S_\xi - \left\langle M\tilde{\boldsymbol{F}},\nabla_\xi\varphi_\Phi\right\rangle_{E,N}, \tag{48a}$$

$$\left\langle\mathcal{J}\vec{F},\vec{\varphi}_F\right\rangle_{E,N} = \int_{\partial E,N}W^\star\tilde{\boldsymbol{\varphi}}_F\cdot\hat{\boldsymbol{n}}\,\mathrm{d}S_\xi - \langle W,\nabla_\xi\cdot\tilde{\boldsymbol{\varphi}}_F\rangle_{E,N}, \tag{48b}$$

$$\langle\mathcal{J}W,\varphi_W\rangle_{E,N} = \left\langle\mathcal{J}\frac{\mathrm{d}\Psi}{\mathrm{d}\Phi},\varphi_W\right\rangle_{E,N} - k\int_{\partial E,N}\varphi_W\,\tilde{\mathbf{Q}}^\star\cdot\hat{\boldsymbol{n}}\,\mathrm{d}S_\xi + k\left\langle\tilde{\mathbf{Q}},\nabla_\xi\varphi_W\right\rangle_{E,N}, \tag{48c}$$

$$\left\langle\mathcal{J}\vec{\mathrm{Q}},\vec{\varphi}_Q\right\rangle_{E,N} = \int_{\partial E,N}\Phi^\star\tilde{\boldsymbol{\varphi}}_Q\cdot\hat{\boldsymbol{n}}\,\mathrm{d}S_\xi - \langle\Phi,\nabla_\xi\cdot\tilde{\boldsymbol{\varphi}}_Q\rangle_{E,N}. \tag{48d}$$

The terms with star superscript in (48) are the *numerical fluxes*, which make the flux uniquely defined at the boundaries. The DG variant implemented depends on the choice of the numerical fluxes. In this work, we use the Bassi–Rebay 1 scheme (BR1) [24],

$$W^\star = \{\!\{W\}\!\}, \Phi^\star = \{\!\{\Phi\}\!\}, \tag{49}$$

where

$$\{\!\{U\}\!\} = \frac{U^{\partial e^+} + U^{\partial e^-}}{2}, \quad \left\{\!\!\left\{\vec{F}\right\}\!\!\right\} = \frac{\vec{F}^{\partial e^+} + \vec{F}^{\partial e^-}}{2}, \tag{50}$$

is the average operator. For the divergence weak forms, we use the average for $\vec{Q}^\star$ (i.e. the BR1 method). For $\left(M\vec{F}\right)^\star$ we propose the use of the average with additional interface dissipation,

$$\left(M\vec{F}\right)^\star = \left\{\!\!\left\{M\vec{F}\right\}\!\!\right\} - \sigma M [\![W]\!], \vec{Q}^\star = \left\{\!\!\left\{\vec{Q}\right\}\!\!\right\}, \tag{51}$$

where σ is a positive penalty parameter ($\sigma \geqslant 0$). The jump operators (with built–in normal vectors) for a scalar U and a vector $\vec{F}$ are defined as

$$[\![U]\!] = U\vec{n}\big|^{\partial e^+} + U\vec{n}\big|^{\partial e^-}, \quad [\![\vec{F}]\!] = \vec{F}\cdot\vec{n}\big|^{\partial e^+} + \vec{F}\cdot\vec{n}\big|^{\partial e^-}. \tag{52}$$

They satisfy the algebraic identity,

$$[\![U\vec{F}]\!] = \{\!\{U\}\!\}[\![\vec{F}]\!] + [\![U]\!]\cdot\left\{\!\!\left\{\vec{F}\right\}\!\!\right\}. \tag{53}$$

For the penalty parameter σ, we propose to use the estimate introduced for the DGSEM–GL variant in [25],

$$\sigma = \kappa_\sigma \frac{N(N+1)}{2} |\mathcal{J}_f| \left\{\!\!\left\{\mathcal{J}^{-1}\right\}\!\!\right\}, \tag{54}$$

which has only one dimensionless free parameter, κ_σ (also positive), and the dependency of σ on the mesh and the polynomial order are taken into account explicitly. In (54), N is the polynomial order, $|\mathcal{J}_f|$ is the surface Jacobian of the face, and $\left\{\!\!\left\{\mathcal{J}^{-1}\right\}\!\!\right\}$ is the average of the inverse of the Jacobians of the elements that share the face evaluated at the face. It will be shown that the scheme is stable without interface stabilization. Nevertheless, the advantage of adding interface stabilization will be demonstrated with a numerical test. We have not introduced dissipation in $\vec{Q}^\star$ since it generates non–physical terms in the discrete free–energy, see Appendix B.

For Neumann boundary conditions, we use the adjacent element interior value to compute gradients in (48b) and (48d),

$$W^\star = W\big|_{\partial e}, \quad \Phi^\star = \Phi\big|_{\partial e}, \tag{55}$$

and directly impose Neumann boundary values for divergence weak forms (48a) and (48c),

$$\left(M\vec{F}\right)^\star\cdot\vec{n} = 0, \quad \vec{Q}^\star\cdot\vec{n} = \frac{\mathrm{d}G\left(\Phi\big|_{\partial e}\right)}{\mathrm{d}\phi} = \beta. \tag{56}$$

Note that we have written the physical interface fluxes, rather than the contravariant fluxes, so that we can more easily relate the interface values shared by two elements (recall that the same physical flux yields different contravariant flux values, as it depends on each element geometry).

4. Stability analysis

In this section, we will follow the steps in Sec. 2.1 for the continuous analysis to show the stability of the numerical scheme (48). We first show in Sec. 4.1 the semi–discrete free–energy estimate assuming exact time integration. Then, in Sec. 4.2 we do the same for a fully discrete approximation in space and time.

4.1. Semi–discrete stability analysis

In this section we follow the steps used to derive the free–energy bound (21) to derive an equivalent discrete bound for a modification of (11d) assuming exact time integration.

Following the continuous analysis, we first take the (exact) time derivative of (11d),

$$\left\langle \mathcal{J}\vec{Q}_t, \vec{\varphi}_Q \right\rangle_{E,N} = \int_{\partial E,N} \Phi_t^\star \tilde{\boldsymbol{\varphi}}_Q\cdot\hat{\boldsymbol{n}}\,\mathrm{d}S_\xi - \left\langle \Phi_t, \nabla_\xi\cdot\tilde{\boldsymbol{\varphi}}_Q \right\rangle_{E,N}, \tag{57}$$

where we omitted the test function time derivative terms since (11d) holds for any polynomial test function ($\boldsymbol{\varphi}_Q$ or $\boldsymbol{\varphi}_{Q,t}$),

$$\left\langle \mathcal{J}\vec{Q}, \vec{\varphi}_{Q,t} \right\rangle_{E,N} = \int_{\partial E,N} \Phi^\star \tilde{\boldsymbol{\varphi}}_{Q,t} \cdot \hat{\boldsymbol{n}} \, \mathrm{d}S_\xi - \left\langle \Phi, \nabla_\xi \cdot \tilde{\boldsymbol{\varphi}}_{Q,t} \right\rangle_{E,N} . \tag{58}$$

Next, we use the summation–by–parts property (42) in (57),

$$\left\langle \mathcal{J}\vec{Q}_t, \vec{\varphi}_Q \right\rangle_{E,N} = \int_{\partial E,N} \left(\Phi_t^\star - \Phi_t\right) \tilde{\boldsymbol{\varphi}}_Q \cdot \tilde{\boldsymbol{n}} \, \mathrm{d}S_\xi + \left\langle \nabla_\xi \Phi_t, \tilde{\boldsymbol{\varphi}}_Q \right\rangle_{E,N} , \tag{59}$$

and replace $\vec{\varphi}_Q = \vec{Q}$ (and $\tilde{\vec{\varphi}}_{\vec{Q}} = \boldsymbol{\mathcal{M}}^T \vec{\varphi}_{\vec{Q}}$ as shown in (47)), to get the time derivative,

$$\left\langle \mathcal{J}\vec{Q}_t, \vec{Q} \right\rangle_{E,N} = \frac{1}{2}\frac{\mathrm{d}}{\mathrm{d}t} ||\vec{Q}||^2_{J,N} = \int_{\partial E,N} \left(\Phi_t^\star - \Phi_t\right) \tilde{\boldsymbol{Q}} \cdot \tilde{\boldsymbol{n}} \, \mathrm{d}S_\xi + \left\langle \nabla_\xi \Phi_t, \tilde{\boldsymbol{Q}} \right\rangle_{E,N} . \tag{60}$$

We then set $\varphi_W = \Phi_t$ in (48c),

$$\langle \mathcal{J}W, \Phi_t \rangle_{E,N} = \left\langle \mathcal{J}\frac{\mathrm{d}\Psi}{\mathrm{d}\Phi}, \Phi_t \right\rangle_{E,N} - k \int_{\partial E,N} \Phi_t \tilde{\boldsymbol{Q}}^\star \cdot \hat{\boldsymbol{n}} \, \mathrm{d}S_\xi + k \left\langle \tilde{\boldsymbol{Q}}, \nabla_\xi \Phi_t \right\rangle_{E,N} . \tag{61}$$

Since the time derivative is exact, we can use the chain rule for the chemical free–energy potential derivative,

$$\left\langle \mathcal{J}\frac{\mathrm{d}\Psi}{\mathrm{d}\Phi}, \Phi_t \right\rangle_{E,N} = \frac{\mathrm{d}}{\mathrm{d}t} \langle \mathcal{J}\Psi, 1 \rangle_{E,N} . \tag{62}$$

We subtract (60) multiplied by k from (61), and use the result in (62) to obtain,

$$\langle \mathcal{J}W, \Phi_t \rangle_{E,N} = \frac{\mathrm{d}}{\mathrm{d}t} \langle \mathcal{J}\Psi, 1 \rangle_{E,N} + \frac{k}{2}\frac{\mathrm{d}}{\mathrm{d}t} ||Q||^2_{J,N} - k \int_{\partial E,N} \left(\Phi_t \tilde{\boldsymbol{Q}}^\star \cdot \hat{\boldsymbol{n}} + \Phi_t^\star \tilde{\boldsymbol{Q}} \cdot \hat{\boldsymbol{n}} - \Phi_t \tilde{\boldsymbol{Q}} \cdot \hat{\boldsymbol{n}} \right) \mathrm{d}S_\xi . \tag{63}$$

Next, we use the summation–by–parts property (42) again in (48b),

$$\left\langle \mathcal{J}\vec{F}, \vec{\varphi}_F \right\rangle_{E,N} = \int_{\partial E,N} \left(W^\star - W\right) \tilde{\boldsymbol{\varphi}}_F \cdot \hat{\boldsymbol{n}} \, \mathrm{d}S_\xi + \left\langle \nabla_\xi W, \tilde{\boldsymbol{\varphi}}_F \right\rangle_{E,N} , \tag{64}$$

and we set $\vec{\varphi}_F = M\vec{F}$, so that

$$\left\langle \mathcal{J}\vec{F}, M\vec{F} \right\rangle_{E,N} = \left|\left| \sqrt{M}\vec{F} \right|\right|^2_{J,N} = \int_{\partial E,N} \left(W^\star - W\right) M\tilde{\boldsymbol{F}} \cdot \hat{\boldsymbol{n}} \, \mathrm{d}S_\xi + \left\langle \nabla_\xi W, M\tilde{\boldsymbol{F}} \right\rangle_{E,N} . \tag{65}$$

Lastly, we set $\varphi_\Phi = W$ in (48a),

$$\langle \mathcal{J}\Phi_t, W \rangle_{E,N} = \int_{\partial E,N} W \left(M\tilde{\boldsymbol{F}}\right)^\star \cdot \hat{\boldsymbol{n}} \, \mathrm{d}S_\xi - \left\langle M\tilde{\boldsymbol{F}}, \nabla_\xi W \right\rangle_{E,N} , \tag{66}$$

and we sum (65) and (66) to find that

$$\langle \mathcal{J}\Phi_t, W \rangle_{E,N} = \int_{\partial E,N} \left(W \left(M\tilde{\boldsymbol{F}}\right)^\star \cdot \hat{\boldsymbol{n}} + W^\star \left(M\tilde{\boldsymbol{F}}\right) \cdot \hat{\boldsymbol{n}} - W \left(M\tilde{\boldsymbol{F}}\right) \cdot \hat{\boldsymbol{n}} \right) \mathrm{d}S_\xi - \left|\left| \sqrt{M}\vec{F} \right|\right|^2_{J,N} . \tag{67}$$

Now, (63) and (67) both contain the term $\langle \mathcal{J}W, \Phi_t \rangle_{E,N}$ on the left hand side, so we can equate both right hand sides to obtain

$$\begin{aligned} &\int_{\partial E,N} \left(W \left(M\tilde{\boldsymbol{F}}\right)^\star \cdot \hat{\boldsymbol{n}} + W^\star \left(M\tilde{\boldsymbol{F}}\right) \cdot \hat{\boldsymbol{n}} - W \left(M\tilde{\boldsymbol{F}}\right) \cdot \hat{\boldsymbol{n}} \right) \mathrm{d}S_\xi - \left|\left| \sqrt{M}\vec{F} \right|\right|^2_{J,N} \\ &= \frac{\mathrm{d}}{\mathrm{d}t} \langle \mathcal{J}\Psi, 1 \rangle_{E,N} + \frac{k}{2}\frac{\mathrm{d}}{\mathrm{d}t} ||Q||^2_{J,N} - k \int_{\partial E,N} \left(\Phi_t \tilde{\boldsymbol{Q}}^\star \cdot \hat{\boldsymbol{n}} + \Phi_t^\star \tilde{\boldsymbol{Q}} \cdot \hat{\boldsymbol{n}} - \Phi_t \tilde{\boldsymbol{Q}} \cdot \hat{\boldsymbol{n}} \right) \mathrm{d}S_\xi . \end{aligned} \tag{68}$$

Rearranging (68) to move time derivatives to the left hand side of the equation, we get

$$\frac{\mathrm{d}}{\mathrm{d}t}\left(\langle \mathcal{J}\Psi,1\rangle_{E,N}+\frac{k}{2}\left|\left|\vec{Q}\right|\right|_{J,N}^{2}\right)=-\left|\left|\sqrt{M}\vec{F}\right|\right|_{J,N}^{2}+k\mathrm{BT}_{E,N}(\Phi_t,\vec{Q})+\mathrm{BT}_{E,N}(W,M\vec{F}). \tag{69}$$

In (69) we used the boundary operator defined as (in both physical and computational spaces according to (45)),

$$\mathrm{BT}_{E,N}\left(\vartheta,\vec{\tau}\right)=\int_{\partial E,N}\left(\vartheta\,\tilde{\boldsymbol{\tau}}^{\star}+\left(\vartheta^{\star}-\vartheta\right)\tilde{\boldsymbol{\tau}}\right)\cdot\hat{\boldsymbol{n}}\,\mathrm{d}S_{\xi}=\int_{\partial e,N}\left(\vartheta\,\vec{\tau}^{\star}+\left(\vartheta^{\star}-\vartheta\right)\vec{\tau}\right)\cdot\vec{n}\,\mathrm{d}S. \tag{70}$$

Additionally, we identify the volumetric discrete free–energy of the element,

$$\frac{\mathrm{d}}{\mathrm{d}t}\left(\langle \mathcal{J}\Psi,1\rangle_{E,N}+\frac{k}{2}\left|\left|\vec{Q}\right|\right|_{J,N}^{2}\right)=\frac{\mathrm{d}}{\mathrm{d}t}\int_{E,N}\mathcal{J}\left(\Psi+\frac{k}{2}\vec{Q}\cdot\vec{Q}\right)dE=\frac{\mathrm{d}\mathcal{F}_{v}^{E,N}}{\mathrm{d}t}, \tag{71}$$

and thus, we simplify (69) to

$$\frac{\mathrm{d}\mathcal{F}_{v}^{E,N}}{\mathrm{d}t}=-\left|\left|\sqrt{M}\vec{F}\right|\right|_{J,N}^{2}+k\mathrm{BT}_{E,N}(\Phi_t,\vec{Q})+\mathrm{BT}_{E,N}(W,M\vec{F}). \tag{72}$$

In (72), we find that the volumetric free–energy is dissipated in the element interior by the chemical potential flux (similarly to the continuous counterpart (20)), and exchanged with other elements through the boundary terms $\mathrm{BT}_{E,N}$.

To obtain an energy estimate similar to that in (21), we sum all element contributions, getting

$$\sum_{e}\frac{\mathrm{d}\mathcal{F}_{v}^{E,N}}{\mathrm{d}t}=\frac{\mathrm{d}\mathcal{F}_{v}^{N}}{\mathrm{d}t}=-\sum_{e}\left|\left|\sqrt{M}\vec{F}\right|\right|_{J,N}^{2}+\sum_{e}\left(k\mathrm{BT}_{E,N}(\Phi_t,\vec{Q})+\mathrm{BT}_{E,N}(W,M\vec{F})\right). \tag{73}$$

We then split the boundary quadratures $\sum_e \mathrm{BT}_{E,N}=\mathrm{IBT}_N+\mathrm{PBT}_N$ into the combination of interior (IBT_N) and physical boundary (PBT_N) sums. We first transform the sums to physical coordinates using (45),

$$\begin{aligned}
&k\mathrm{BT}_{E,N}(\Phi_t,\vec{Q})+\mathrm{BT}_{E,N}(W,M\vec{F})\\
&\quad=k\int_{\partial E,N}\left(\Phi_t\,\tilde{\boldsymbol{Q}}^{\star}\cdot\hat{\boldsymbol{n}}+\Phi_t^{\star}\,\tilde{\boldsymbol{Q}}\cdot\hat{\boldsymbol{n}}-\Phi_t\,\tilde{\boldsymbol{Q}}\cdot\hat{\boldsymbol{n}}\right)\mathrm{d}S_{\xi}\\
&\qquad+\int_{\partial E,N}\left(W\left(M\tilde{\boldsymbol{F}}\right)^{\star}\cdot\hat{\boldsymbol{n}}+W^{\star}\left(M\tilde{\boldsymbol{F}}\right)\cdot\hat{\boldsymbol{n}}-W\left(M\tilde{\boldsymbol{F}}\right)\cdot\hat{\boldsymbol{n}}\right)\mathrm{d}S_{\xi}\\
&\quad=k\int_{\partial e,N}\left(\Phi_t\vec{Q}^{\star}\cdot\vec{n}+\Phi_t^{\star}\vec{Q}\cdot\vec{n}-\Phi_t\vec{Q}\cdot\vec{n}\right)\mathrm{d}S\\
&\qquad+\int_{\partial e,N}\left(W\left(M\vec{F}\right)^{\star}\cdot\vec{n}+W^{\star}\left(M\vec{F}\right)\cdot\vec{n}-W\left(M\vec{F}\right)\cdot\vec{n}\right)\mathrm{d}S.
\end{aligned} \tag{74}$$

At interior faces there is a contribution from the left and the right sides. We account for the contribution of the two neighboring elements in the following way: if E^{+} and E^{-} are two elements that share a face f, the sum of both contributions to the face is

$$\begin{aligned}
\int_{f,N}\left(\tilde{\vec{F}}\cdot\hat{\vec{n}}\Big|^{\partial e^{+}}+\tilde{\vec{F}}\cdot\hat{\vec{n}}\Big|^{\partial e^{-}}\right)\mathrm{d}S_{\xi}&=\int_{f,N}\left(\vec{F}\cdot\vec{n}\Big|^{\partial e^{+}}+\vec{F}\cdot\vec{n}\Big|^{\partial e^{-}}\right)\mathrm{d}S\\
&=\int_{f,N}[\![\vec{F}]\!]\,\mathrm{d}S.
\end{aligned} \tag{75}$$

Using the definitions for the jumps at an interface between two elements, the face contributions to the sum over all elements of the boundary terms can be written as

$$\begin{aligned}
\mathrm{IBT}_N=&k\sum_{\substack{\text{interior}\\ \text{faces}}}\int_{f,N}\left(\left[\!\left[\Phi_t\vec{Q}^{\star}\right]\!\right]+\left[\!\left[\Phi_t^{\star}\vec{Q}\right]\!\right]-\left[\!\left[\Phi_t\vec{Q}\right]\!\right]\right)\mathrm{d}S\\
&+\sum_{\substack{\text{interior}\\ \text{faces}}}\int_{f,N}\left(\left[\!\left[W\left(M\vec{F}\right)^{\star}\right]\!\right]+\left[\!\left[W^{\star}M\vec{F}\right]\!\right]-\left[\!\left[WM\vec{F}\right]\!\right]\right)\mathrm{d}S.
\end{aligned} \tag{76}$$

Since interface numerical fluxes are uniquely defined at the interfaces, as noted in (51), we can remove them from the jump operator so

$$\begin{aligned}\mathrm{IBT}_N = k &\sum_{\substack{\text{interior}\\ \text{faces}}} \int_{f,N} \left(\vec{Q}^{\star} \cdot [\![\Phi_t]\!] + \Phi_t^{\star} \left[\!\left[\vec{Q} \right]\!\right] - \left[\!\left[\Phi_t \vec{Q} \right]\!\right] \right) \mathrm{d}S \\ + &\sum_{\substack{\text{interior}\\ \text{faces}}} \int_{f,N} \left(\left(M\vec{F} \right)^{\star} \cdot [\![W]\!] + W^{\star} \left[\!\left[M\vec{F} \right]\!\right] - \left[\!\left[W M\vec{F} \right]\!\right] \right) \mathrm{d}S.\end{aligned} \tag{77}$$

To show stability, we replace the numerical fluxes in (77) with the averages of the BR1 method (see (49) and (51)),

$$\begin{aligned}\mathrm{IBT}_N = k &\sum_{\substack{\text{interior}\\ \text{faces}}} \int_{f,N} \left(\left\{\!\left\{ \vec{Q} \right\}\!\right\} \cdot [\![\Phi_t]\!] + \{\!\{\Phi_t\}\!\} \left[\!\left[\vec{Q} \right]\!\right] - \left[\!\left[\Phi_t \vec{Q} \right]\!\right] \right) \mathrm{d}S \\ + &\sum_{\substack{\text{interior}\\ \text{faces}}} \int_{f,N} \left(\left\{\!\left\{ M\vec{F} \right\}\!\right\} \cdot [\![W]\!] + \{\!\{W\}\!\} \left[\!\left[M\vec{F} \right]\!\right] - \left[\!\left[W M\vec{F} \right]\!\right] \right) \mathrm{d}S \\ - &\sum_{\substack{\text{interior}\\ \text{faces}}} \int_{f,N} \sigma M [\![W]\!]^2 \, \mathrm{d}S = - \sum_{\substack{\text{interior}\\ \text{faces}}} \int_{f,N} \sigma M [\![W]\!]^2 \, \mathrm{d}S.\end{aligned} \tag{78}$$

The two first sums in (78) vanish by the algebraic identity (53), and the third is always negative. As a result, the contribution from interior faces only maintains or decreases the free–energy (or does not contribute if $\sigma = 0$).

For the physical boundary terms,

$$\begin{aligned}\mathrm{PBT}_N = k &\sum_{\substack{\text{boundary}\\ \text{faces}}} \int_{f,N} \left(\Phi_t \tilde{\boldsymbol{Q}}^{\star} \cdot \hat{\boldsymbol{n}} + \Phi_t^{\star} \tilde{\boldsymbol{Q}} \cdot \hat{\boldsymbol{n}} - \Phi_t \tilde{\boldsymbol{Q}} \cdot \hat{\boldsymbol{n}} \right) \mathrm{d}S_{\xi} \\ + &\sum_{\substack{\text{boundary}\\ \text{faces}}} \int_{f,N} \left(W \left(M\tilde{\boldsymbol{F}} \right)^{\star} \cdot \hat{\boldsymbol{n}} + W^{\star} \left(M\tilde{\boldsymbol{F}} \right) \cdot \hat{\boldsymbol{n}} - W \left(M\tilde{\boldsymbol{F}} \right) \cdot \hat{\boldsymbol{n}} \right) \mathrm{d}S_{\xi},\end{aligned} \tag{79}$$

we set the values specified in (55) and (56), and as a result, the second quadrature vanishes. In the first quadrature we can use the chain rule in time to see that

$$\mathrm{PBT}_N = k \sum_{\substack{\text{boundary}\\ \text{faces}}} \int_{f,N} \Phi_t \frac{\mathrm{d}G}{\mathrm{d}\phi} \mathrm{d}S = \frac{\mathrm{d}}{\mathrm{d}t} \left(k \sum_{\substack{\text{boundary}\\ \text{faces}}} \int_{f,N} G(\Phi) \, \mathrm{d}S \right) = - \frac{\mathrm{d}\mathcal{F}_s^N}{\mathrm{d}t}. \tag{80}$$

Hence, we can rewrite (73) to mimic the continuous free–energy bound (20),

$$\begin{aligned}\frac{\mathrm{d}\mathcal{F}_v^N}{\mathrm{d}t} + \frac{\mathrm{d}\mathcal{F}_s^N}{\mathrm{d}t} = \frac{\mathrm{d}\mathcal{F}^N}{\mathrm{d}t} &= - \sum_e \left|\left| \sqrt{M}\vec{F} \right|\right|_{J,N}^2 - \sum_{\substack{\text{interior}\\ \text{faces}}} \int_{f,N} \sigma M [\![W]\!]^2 \, \mathrm{d}S \\ &\leqslant - \sum_e \left|\left| \sqrt{M}\vec{F} \right|\right|_{J,N}^2 \leqslant 0.\end{aligned} \tag{81}$$

When integrated in time, we obtain the semi–discrete version of (21),

$$\mathcal{F}^N(T) \leqslant \mathcal{F}^N(0) - \int_0^T \left(\sum_e \left|\left| \sqrt{M}\vec{F} \right|\right|_{J,N}^2 \right) dt \leqslant \mathcal{F}^N(0), \tag{82}$$

where we recall that the numerical errors incurred at the interior boundaries IBT_N are zero for the BR1 scheme ($\sigma = 0$), and dissipative otherwise ($\sigma > 0$).

Therefore, the semi–discrete DG scheme (48) is stable, in the sense that the discrete free–energy,

$$\mathcal{F}^N = \sum_e \left\{ \int_{E,N} \mathcal{J} \left(\Psi + \frac{1}{2} k \vec{Q} \cdot \vec{Q} \right) dE - \int_{\partial e \bigcap \partial\Omega,N} G(\Phi) \, \mathrm{d}S \right\}, \tag{83}$$

is bounded in time by its initial value.

4.2. Fully–discrete stability analysis using an IMEX time integrator

Because of the stiffness due to the high order derivatives in the Cahn-Hilliard equation, we use an IMplicit–EXplicit (IMEX) time integrator. We consider equally–spaced time steps Δt and we use the superscript n to represent state values in $t_n = n\Delta t$,

$$\vartheta^n = \vartheta(t_n) = \vartheta(n\Delta t). \tag{84}$$

In particular, this IMplicit–EXplicit (IMEX) solver combines a forward and backward Euler scheme. We split the equations into implicit and explicit parts to make the algebraic system that needs to be solved linear, despite the original equation being non–linear, so that its solution can be found with a fast, efficient direct linear solver.

We recall the spatially continuous PDE to emphasize the time discretization now

$$\phi_t = \nabla\cdot(M\nabla w) = \nabla\cdot\left(M\nabla\left(\psi(\phi) - k\nabla^2\phi\right)\right). \tag{85}$$

Integrating over one time–step $t\in[t_n, t_{n+1}]$, we find,

$$\int_{t_n}^{t_{n+1}} \phi_t dt = \phi^{n+1} - \phi^n = \int_{t_n}^{t_{n+1}} \nabla\cdot\left(M\nabla\left(\frac{\mathrm{d}\psi(\phi)}{\mathrm{d}\phi} - k\nabla^2\phi\right)\right) dt. \tag{86}$$

Depending on whether we evaluate the right hand side of (86) at t_n or t_{n+1} we obtain forward (explicit) and backward (implicit) Euler schemes respectively.

On the one hand, the interface energy term $k\nabla^2\phi$ needs to be implicit, since otherwise explicit time integration requires an impractical time–step restriction. On the other hand, the chemical free–energy term $\psi(\phi)$ is nonlinear and is more easily treated explicitly. For these reasons, we evaluate (86) in time as

$$\phi^{n+1} - \phi^n = \Delta t\nabla\cdot\left(M\nabla\left(\frac{\mathrm{d}\psi(\phi^n)}{\mathrm{d}\phi} - k\nabla^2\phi^{n+1}\right)\right). \tag{87}$$

The time integration scheme (87) is not provably stable because of the non–linearities in the chemical free–energy. Following [18], we modify the chemical potential adding numerical stabilization proportional to solution time jumps $\Delta\phi = \phi^{n+1} - \phi^n$,

$$\phi^{n+1} - \phi^n = \Delta t\nabla\cdot\left(M\nabla\left(\frac{\mathrm{d}\psi(\phi^n)}{\mathrm{d}\phi} + S_0\left(\phi^{n+1} - \phi^n\right) - k\nabla^2\phi^{n+1}\right)\right), \tag{88}$$

where S_0 is a constant, which maintains first order accuracy and makes it possible to obtain a stable scheme.

In Appendix A, we also address the stability of explicit–Euler and the Crank–Nicolson scheme. We replace Φ^{n+1} by a linear blending with coefficient K_0 in the two timesteps for the interfacial energy in (88),

$$\phi^{n+1} - \phi^n = \Delta t\nabla\cdot\left(M\nabla\left(\frac{\mathrm{d}\psi(\phi^n)}{\mathrm{d}\phi} + S_0\Delta\phi - k\nabla^2\left(K_0\phi^{n+1} + (1-K_0)\phi^n\right)\right)\right), \tag{89}$$

so that $K_0 = 0$ is explicit Euler, $K_0 = 1/2$ is the Crank–Nicolson scheme, and $K_0 = 1$ is implicit Euler.

We introduce the time discretization (88) into (48) to obtain the fully–discrete discontinuous Galerkin approximation,

$$\left\langle \mathcal{J}\frac{\Phi^{n+1} - \Phi^n}{\Delta t}, \varphi_\Phi\right\rangle_{E,N} = \int_{\partial E,N} \varphi_\Phi\left(M\tilde{\boldsymbol{F}}\right)^{\star,\theta}\cdot\hat{\boldsymbol{n}}\,\mathrm{d}S_\xi - \left\langle M\tilde{\boldsymbol{F}}^\theta, \nabla_\xi\varphi_\Phi\right\rangle_{E,N}, \tag{90a}$$

$$\left\langle \mathcal{J}\vec{F}^\theta, \vec{\varphi}_F\right\rangle_{E,N} = \int_{\partial E,N}\left(W^{\star,\theta} - W^\theta\right)\tilde{\boldsymbol{\varphi}}_F\cdot\hat{\boldsymbol{n}}\,\mathrm{d}S_\xi + \left\langle\nabla_\xi W^\theta, \tilde{\boldsymbol{\varphi}}_F\right\rangle_{E,N}, \tag{90b}$$

$$\begin{aligned}\left\langle \mathcal{J}W^\theta, \varphi_W\right\rangle_{E,N} =& \left\langle\left(\frac{\mathrm{d}\Psi}{\mathrm{d}\Phi}\right)^n + S_0\left(\Phi^{n+1} - \Phi^n\right), \mathcal{J}\varphi_W\right\rangle_{E,N}\\ &- k\int_{\partial E,N}\varphi_W\,\tilde{\boldsymbol{Q}}^{\star,n+1}\cdot\hat{\boldsymbol{n}}\,\mathrm{d}S_\xi + k\left\langle\tilde{\boldsymbol{Q}}^{n+1}, \nabla_\xi\varphi_W\right\rangle_{E,N},\end{aligned} \tag{90c}$$

$$\left\langle \mathcal{J}\vec{Q}^{n+1}, \vec{\varphi}_Q\right\rangle_{E,N} = \int_{\partial E,N}\left(\Phi^{\star,n+1} - \Phi^{n+1}\right)\tilde{\boldsymbol{\varphi}}_Q\cdot\hat{\boldsymbol{n}}\,\mathrm{d}S_\xi + \left\langle\nabla_\xi\Phi^{n+1}, \tilde{\boldsymbol{\varphi}}_Q\right\rangle_{E,N}, \tag{90d}$$

where we use the superscript θ for variables (e.g. $\vec{F}^{\theta}$ or W^{θ}) that are not directly evaluated at t_n or t_{n+1} with the IMEX strategy, but on a combination of those depending on the different terms involved in (90c). Moreover, following the semi–discrete analysis, we have already applied the summation–by–parts property (42) in (90b) and (90d).

To analyze the stability of the system (90), we start by combining (90c) and (90d). We perform the first manipulations on (90d), which we set for both t_{n+1} and t_n,

$$\left\langle \mathcal{J}\vec{Q}^{n+1}, \vec{\varphi}_Q \right\rangle_{E,N} = \int_{\partial E,N} \left(\Phi^{\star,n+1} - \Phi^{n+1}\right) \tilde{\boldsymbol{\varphi}}_Q \cdot \hat{\boldsymbol{n}} \, \mathrm{d}S_\xi + \left\langle \nabla_\xi \Phi^{n+1}, \tilde{\boldsymbol{\varphi}}_Q \right\rangle_{E,N}, \tag{91a}$$

$$\left\langle \mathcal{J}\vec{Q}^{n}, \vec{\varphi}_Q \right\rangle_{E,N} = \int_{\partial E,N} \left(\Phi^{\star,n} - \Phi^{n}\right) \tilde{\boldsymbol{\varphi}}_Q \cdot \hat{\boldsymbol{n}} \, \mathrm{d}S_\xi + \left\langle \nabla_\xi \Phi^{n}, \tilde{\boldsymbol{\varphi}}_Q \right\rangle_{E,N}. \tag{91b}$$

Then we subtract (91b) from (91a), divide the result by Δt (note that we have defined $\Delta\Phi = \Phi^{n+1} - \Phi^n$ and $\Delta\vec{Q} = \vec{Q}^{n+1} - \vec{Q}^n$),

$$\left\langle \mathcal{J}\frac{\Delta\vec{Q}}{\Delta t}, \vec{\varphi}_Q \right\rangle_{E,N} = \int_{\partial E,N} \left(\frac{\Delta\Phi^{\star}}{\Delta t} - \frac{\Delta\Phi}{\Delta t}\right) \tilde{\boldsymbol{\varphi}}_Q \cdot \hat{\boldsymbol{n}} \, \mathrm{d}S_\xi + \left\langle \frac{\nabla_\xi\left(\Delta\Phi\right)}{\Delta t}, \tilde{\boldsymbol{\varphi}}_Q \right\rangle_{E,N}, \tag{92}$$

and we set $\vec{\varphi}_Q = \vec{Q}^{n+1}$ in (92) to obtain

$$\left\langle \mathcal{J}\frac{\Delta\vec{Q}}{\Delta t}, \vec{Q}^{n+1} \right\rangle_{E,N} = \int_{\partial E,N} \left(\frac{\Delta\Phi^{\star}}{\Delta t} - \frac{\Delta\Phi}{\Delta t}\right) \tilde{\boldsymbol{Q}}^{n+1} \cdot \hat{\boldsymbol{n}} \, \mathrm{d}S_\xi + \left\langle \frac{\nabla_\xi\left(\Delta\Phi\right)}{\Delta t}, \tilde{\boldsymbol{Q}}^{n+1} \right\rangle_{E,N}. \tag{93}$$

Next, we set $\varphi_W = \Delta\Phi/\Delta t = \left(\Phi^{n+1} - \Phi^n\right)/\Delta t$ in (90c),

$$\begin{aligned} \left\langle \mathcal{J}W^{\theta}, \frac{\Delta\Phi}{\Delta t} \right\rangle_{E,N} =& \left\langle \left(\frac{\mathrm{d}\Psi}{\mathrm{d}\Phi}\right)^n + S_0\Delta\Phi, \mathcal{J}\frac{\Delta\Phi}{\Delta t} \right\rangle_{E,N} \\ & - k\int_{\partial E,N} \frac{\Delta\Phi}{\Delta t}\tilde{\boldsymbol{Q}}^{\star,n+1} \cdot \hat{\boldsymbol{n}} \, \mathrm{d}S_\xi + k\left\langle \tilde{\boldsymbol{Q}}^{n+1}, \frac{\nabla_\xi\left(\Delta\Phi\right)}{\Delta t} \right\rangle_{E,N}, \end{aligned} \tag{94}$$

and replace the last inner product in (94) by that in (93),

$$\begin{aligned} \left\langle \mathcal{J}W^{\theta}, \frac{\Delta\Phi}{\Delta t} \right\rangle_{E,N} =& \left\langle \left(\frac{\mathrm{d}\Psi}{\mathrm{d}\Phi}\right)^n + S_0\Delta\Phi, \mathcal{J}\frac{\Delta\Phi}{\Delta t} \right\rangle_{E,N} + k\left\langle \mathcal{J}\frac{\Delta\vec{Q}}{\Delta t}, \vec{Q}^{n+1} \right\rangle_{E,N} \\ & - k\int_{\partial E,N} \left(\frac{\Delta\Phi}{\Delta t}\tilde{\boldsymbol{Q}}^{\star,n+1} \cdot \hat{\boldsymbol{n}} + \left(\frac{\Delta\Phi^{\star} - \Delta\Phi}{\Delta t}\right)\tilde{\boldsymbol{Q}}^{n+1} \cdot \hat{\boldsymbol{n}}\right) \mathrm{d}S_\xi. \end{aligned} \tag{95}$$

Using the boundary operator (70),

$$\begin{aligned} \left\langle \mathcal{J}W^{\theta}, \frac{\Delta\Phi}{\Delta t} \right\rangle_{E,N} =& \left\langle \left(\frac{\mathrm{d}\Psi}{\mathrm{d}\Phi}\right)^n + S_0\Delta\Phi, \mathcal{J}\frac{\Delta\Phi}{\Delta t} \right\rangle_{E,N} + k\left\langle \mathcal{J}\frac{\Delta\vec{Q}}{\Delta t}, \vec{Q}^{n+1} \right\rangle_{E,N} \\ & - k\mathrm{BT}_{E,N}\left(\frac{\Delta\Phi}{\Delta t}, \vec{Q}^{n+1}\right). \end{aligned} \tag{96}$$

Next, we combine (90a) and (90b). To do so, we set $\vec{\varphi}_{\vec{F}} = \mathcal{I}^N\left[M\vec{F}^{\theta}\right]$ in (90b) (note we drop the $\mathcal{I}^N$ operator since the quadrature only requires nodal values, that is $\left\langle \mathcal{I}^N\left(M\vec{F}^{\theta}\right), \vartheta \right\rangle_{E,N} = \left\langle M\vec{F}^{\theta}, \vartheta \right\rangle_{E,N}$),

$$\left\langle \mathcal{J}\vec{F}^{\theta}, M\vec{F}^{\theta} \right\rangle_{E,N} = \int_{\partial E,N} \left(W^{\star,\theta} - W^{\theta}\right) M\tilde{\boldsymbol{F}}^{\theta} \cdot \hat{\boldsymbol{n}} \, \mathrm{d}S_\xi + \left\langle \nabla_\xi W^{\theta}, M\tilde{\boldsymbol{F}}^{\theta} \right\rangle_{E,N}, \tag{97}$$

and we set $\varphi_\Phi = W^{\theta}$ in (90a),

$$\left\langle \mathcal{J}\frac{\Delta\Phi}{\Delta t}, W^{\theta} \right\rangle_{E,N} = \int_{\partial E,N} W^{\theta}\left(M\tilde{\boldsymbol{F}}\right)^{\star,\theta} \cdot \hat{\boldsymbol{n}} \, \mathrm{d}S_\xi - \left\langle M\tilde{\boldsymbol{F}}^{\theta}, \nabla_\xi W^{\theta} \right\rangle_{E,N}. \tag{98}$$

We then sum (97) and (98), and use the boundary term operator (70),

$$\left\langle \mathcal{J}\frac{\Delta\Phi}{\Delta t}, W^\theta \right\rangle_{E,N} = -\left\langle \mathcal{J}\vec{F}^\theta, M\vec{F}^\theta \right\rangle_{E,N} + \mathrm{BT}_{E,N}\left(W^\theta, M\vec{F}^\theta\right). \tag{99}$$

The final step is to combine (96) and (99). Since they share their left hand sides, we equate both right hand sides and multiply them by the time step Δt,

$$\begin{aligned}&\left\langle \left(\frac{\mathrm{d}\Psi}{\mathrm{d}\Phi}\right)^n + S_0\Delta\Phi, \mathcal{J}\Delta\Phi \right\rangle_{E,N} + k\left\langle \mathcal{J}\Delta\vec{Q}, \vec{Q}^{n+1} \right\rangle_{E,N} \\ &= -\Delta t\left\langle \mathcal{J}\vec{F}^\theta, M\vec{F}^\theta \right\rangle_{E,N} + k\mathrm{BT}_{E,N}\left(\Delta\Phi, \vec{Q}^{n+1}\right) + \Delta t\mathrm{BT}_{E,N}\left(W^\theta, M\vec{F}^\theta\right).\end{aligned} \tag{100}$$

We then perform manipulations on the left hand side to get the free–energy $\mathcal{F}$. First, we perform the Taylor expansion of $\Psi(\Phi)$ centered on Φ^n,

$$\Psi^{n+1} = \Psi^n + \left(\frac{\mathrm{d}\Psi}{\mathrm{d}\Phi}\right)^n \Delta\Phi + \frac{1}{2}\left(\frac{\mathrm{d}^2\Psi}{\mathrm{d}\Phi^2}\right)^n \Delta\Phi^2 + \frac{1}{6}\left(\frac{\mathrm{d}^3\Psi}{\mathrm{d}\Phi^3}\right)^n \Delta\Phi^3 + \frac{1}{24}\left(\frac{\mathrm{d}^4\Psi}{\mathrm{d}\Phi^4}\right)^n \Delta\Phi^4 + \dots \tag{101}$$

For the polynomic chemical energy, (9),

$$(d\Psi/d\Phi)^n = -\Phi^n + \left(\Phi^n\right)^3, \tag{102}$$

$$\left(d^2\Psi/d\Phi^2\right)^n = -1 + 3\left(\Phi^n\right)^2, \tag{103}$$

$$\left(d^3\Psi/d\Phi^3\right)^n = 6\Phi^n, \tag{104}$$

and

$$\left(d^4\Psi/d\Phi^4\right)^n = 6, \tag{105}$$

so, it follows exactly that

$$\Psi^{n+1} = \Psi^n + \left(\frac{\mathrm{d}\Psi}{\mathrm{d}\Phi}\right)^n \Delta\Phi - \frac{1}{2}\left(1 - 3\left(\Phi^n\right)^2\right)\Delta\Phi^2 + \Phi^n\Delta\Phi^3 + \frac{1}{4}\Delta\Phi^4. \tag{106}$$

We use (106) to write the first volume quadrature in (100) as

$$\left\langle \left(\frac{\mathrm{d}\Psi}{\mathrm{d}\Phi}\right)^n + S_0\Delta\Phi, \mathcal{J}\Delta\Phi \right\rangle_{E,N} = \left\langle \mathcal{J}\Psi^{n+1}, 1\right\rangle_{E,N} - \left\langle \mathcal{J}\Psi^n, 1\right\rangle_{E,N} + \left\langle \mathcal{J}\Pi, 1\right\rangle_{E,N}, \tag{107}$$

where $\Pi\left(\Phi^{n+1}, \Phi^n\right)$ is the polynomial function

$$\Pi = S_0\Delta\Phi^2 + \frac{1}{2}\left(1 - 3\left(\Phi^n\right)^2\right)\Delta\Phi^2 - \Phi^n\Delta\Phi^3 - \frac{1}{4}\Delta\Phi^4 = \Delta\Phi^2\Pi^\star, \tag{108}$$

with

$$\Pi^\star = S_0 + \frac{1}{2}\left(1 - 3\left(\Phi^n\right)^2\right) - \Phi^n\left(\Phi^{n+1} - \Phi^n\right) - \frac{1}{4}\left(\Phi^{n+1} - \Phi^n\right)^2. \tag{109}$$

The quantity $\Pi^\star$ is a second order concave polynomial (elliptic paraboloid). For the time integration to be stable, it suffices that $\Pi^\star$ remains positive, as will be inferred from the stability analysis. Since $\Pi^\star$ is a concave function, it will always shift negative for sufficiently large values of Φ^{n+1} or Φ^n. However, acceptable solutions of the Cahn–Hilliard equation remain close to the range $\phi \in [-1, 1]$. Thus, we can choose the value S_0 so that $\Pi^\star$ remains positive in a reasonably large neighborhood of $\left(\Phi^{n+1}, \Phi^n\right) \in [-1, 1]^2$.

The elliptical isocontours $\Pi^\star = 0$ are shown in Fig. 1 for several S_0 values (as labeled on each contour line). A sufficient condition for positiveness is that every pair $\left(\Phi^n, \Phi^{n+1}\right)$ remains inside the $\Pi^\star = 0$ isoline for the given S_0 value. For instance, given the range $\Phi \in [-1, 1]$, the scheme is stable for $S_0 \geqslant 1$, and for $\Phi \in \left[-\sqrt{5/3}, \sqrt{5/3}\right] \simeq [-1.29, 1.29]$, the scheme remains stable for $S_0 \geqslant 2$.

For the interface energy in (100), we complete the square,

$$\left\langle \mathcal{J}\Delta\vec{Q}, \vec{Q}^{n+1} \right\rangle_{E,N} = \frac{1}{2}\left\langle \mathcal{J}\vec{Q}^{n+1}, \vec{Q}^{n+1} \right\rangle_{E,N} - \frac{1}{2}\left\langle \mathcal{J}\vec{Q}^n, \vec{Q}^n \right\rangle_{E,N} + \frac{1}{2}\left\langle \mathcal{J}\Delta\vec{Q}, \Delta\vec{Q}, \right\rangle_{E,N}, \tag{110}$$

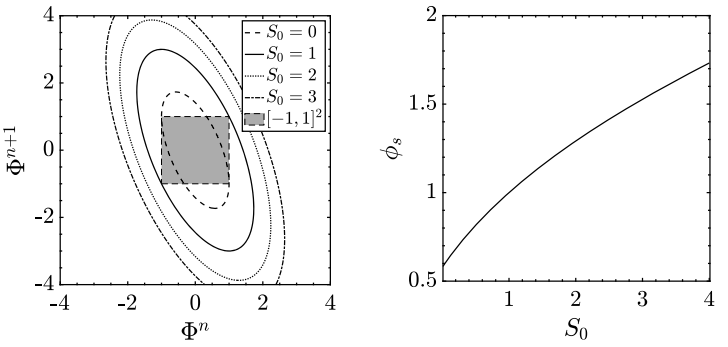

(a) $\Pi^\star = 0$ isolines

(b) Range $\phi \in [-\phi_s, \phi_s]^2$ in which non–linear terms are stable

Fig. 1. Graphical representation of the elliptical isoline $\Pi^\star = 0$ for several S_0 values (indicated by the contour labels). The box $[-1,1]^2$ has also been represented. A sufficient condition for positiveness is that the pair (Φ^n, Φ^{n+1}) stays inside the ellipse for a given S_0 value. In 1(b) we have represented for each S_0 the interval $[-\phi_s, \phi_s]^2$ in which the non–linear terms are stable, which corresponds to the formula $\phi_s = \sqrt{\frac{2S_0+1}{3}}$.

and we place (107) and (110) in (100),

$$\begin{aligned}
&\left\langle \mathcal{J}\left(\Psi^{n+1} + \frac{1}{2}k\vec{Q}^{\,n+1}\cdot\vec{Q}^{\,n+1}\right), 1\right\rangle_{E,N} - \left\langle \mathcal{J}\left(\Psi^{n} + \frac{1}{2}k\vec{Q}^{\,n}\cdot\vec{Q}^{\,n}\right), 1\right\rangle_{E,N} \\
&= -\Delta t\left\langle \mathcal{J}\vec{F}^{\theta}, M\vec{F}^{\theta}\right\rangle_{E,N} + k\mathrm{BT}_{E,N}\left(\Delta\Phi, \vec{Q}^{\,n+1}\right) \\
&+ \Delta t\mathrm{BT}_{E,N}\left(W^{\theta}, M\vec{F}^{\theta}\right) - \langle \mathcal{J}\Pi, 1\rangle_{E,N} - \frac{1}{2}k\left\langle \mathcal{J}\Delta\vec{Q}, \Delta\vec{Q}\right\rangle_{E,N}.
\end{aligned} \tag{111}$$

We define the discrete volumetric free–energy in an element as,

$$\mathcal{F}_v^{n,E,N} = \left\langle \mathcal{J}\left(\Psi^{n} + \frac{1}{2}k\vec{Q}^{\,n}\cdot\vec{Q}^{\,n}\right), 1\right\rangle_{E,N}, \tag{112}$$

which simplifies (111) to

$$\begin{aligned}
\mathcal{F}_v^{n+1,E,N} - \mathcal{F}_v^{n,E,N} =& -\Delta t\left\langle \mathcal{J}\vec{F}^{\theta}, M\vec{F}^{\theta}\right\rangle_{E,N} + k\mathrm{BT}_{E,N}\left(\Delta\Phi, \vec{Q}^{\,n+1}\right) \\
&+ \Delta t\mathrm{BT}_{E,N}\left(W^{\theta}, M\vec{F}^{\theta}\right) - \langle \mathcal{J}\Pi, 1\rangle_{E,N} \\
&- \frac{1}{2}k\left\langle \mathcal{J}\Delta\vec{Q}, \Delta\vec{Q}\right\rangle_{E,N}.
\end{aligned} \tag{113}$$

Eq. (113) shows that free–energy changes are due to physical dissipation in the element interior by the term $\Delta t\left\langle \mathcal{J}\vec{F}^{\theta}, M\vec{F}^{\theta}\right\rangle_{E,N} \geqslant 0$ (the discrete counterpart of that obtained for the continuous analysis (20)), numerical dissipation as a result of the IMEX scheme,

$$\mathrm{diss}_{\mathrm{IMEX}}^{E,N} = -\langle \mathcal{J}\Pi, 1\rangle_{E,N} - \frac{1}{2}k\left\langle \mathcal{J}\Delta\vec{Q}, \Delta\vec{Q}\right\rangle_{E,N} \leqslant 0, \tag{114}$$

and boundary exchanges through all $\mathrm{BT}_{E,N}$ terms.

The effect of boundary exchanges can only be studied from the perspective of all elements in the domain. So we sum (113) for all mesh elements,

$$\mathcal{F}_v^{n+1,N} - \mathcal{F}_v^{n,N} = -\Delta t\sum_e\left\langle \mathcal{J}\vec{F}^{\theta}, M\vec{F}^{\theta}\right\rangle_{E,N} + \mathrm{IBT}_N + \mathrm{PBT}_N + \sum_e \mathrm{diss}_{\mathrm{IMEX}}^{E,N}, \tag{115}$$

where $\mathcal{F}_v^{n,N} = \sum_e \mathcal{F}_v^{n,E,N}$ is the sum of all element volumetric free–energies.

On the one hand, the IBT_N is the contribution of all interior boundary quadratures,

$$\begin{aligned}
\mathrm{IBT}_N =& \sum_{\substack{\text{interior}\\ \text{faces}}}\int_{f,N}\left(M\vec{F}^{\theta,\star}\cdot[\![W^{\theta}]\!] + W^{\theta,\star}\left[\!\left[M\vec{F}^{\theta}\right]\!\right] - \left[\!\left[M\vec{F}^{\theta}W^{\theta}\right]\!\right]\right)\mathrm{d}S \\
&+ k\sum_{\substack{\text{interior}\\ \text{faces}}}\int_{f,N}\left(\vec{Q}^{\,n+1,\star}\cdot[\![\Delta\Phi]\!] + \Delta\Phi^{\star}\left[\!\left[\vec{Q}^{\,n+1}\right]\!\right] - \left[\!\left[\vec{Q}^{\,n+1}\Delta\Phi\right]\!\right]\right)\mathrm{d}S.
\end{aligned} \tag{116}$$

Introducing the numerical fluxes obtained with the BR1 scheme we find that since (53) holds, we obtain the same result as in the semi–discrete analysis (78),

$$\begin{aligned}\mathrm{IBT}_N = & \sum_{\substack{\text{interior}\\ \text{faces}}} \int_{f,N} \left(\left\{\!\!\left\{ M\vec{F}^{\theta} \right\}\!\!\right\} \cdot \left[\!\left[W^{\theta} \right]\!\right] + \left\{\!\!\left\{ W^{\theta} \right\}\!\!\right\} \left[\!\left[M\vec{F}^{\theta} \right]\!\right] - \left[\!\left[M\vec{F}^{\theta} W^{\theta} \right]\!\right] \right) \mathrm{d}S \\ & + k \sum_{\substack{\text{interior}\\ \text{faces}}} \int_{f,N} \left(\left\{\!\!\left\{ \vec{Q}^{\,n+1} \right\}\!\!\right\} \cdot \left[\!\left[\Delta\Phi \right]\!\right] + \left\{\!\!\left\{ \Delta\Phi \right\}\!\!\right\} \left[\!\left[\vec{Q}^{\,n+1} \right]\!\right] - \left[\!\left[\vec{Q}^{\,n+1} \Delta\Phi \right]\!\right] \right) \mathrm{d}S \\ & - \sum_{\substack{\text{interior}\\ \text{faces}}} \int_{f,N} \sigma M \left[\!\left[W^{\theta} \right]\!\right]^2 \mathrm{d}S = - \sum_{\substack{\text{interior}\\ \text{faces}}} \int_{f,N} \sigma M \left[\!\left[W^{\theta} \right]\!\right]^2 \mathrm{d}S. \end{aligned} \tag{117}$$

Therefore, we conclude that the global contribution from interior boundaries to the free–energy changes is stable ($\sigma > 0$), or vanishes ($\sigma = 0$).

On the other hand, we consider the physical boundary terms, PBT_N,

$$\begin{aligned}\mathrm{PBT}_N = & k \sum_{\substack{\text{boundary}\\ \text{faces}}} \int_{f,N} \left(\Delta\Phi\, \tilde{\boldsymbol{Q}}^{\,n+1,\star} \cdot \hat{\boldsymbol{n}} + \Delta\Phi^{\star}\, \tilde{\boldsymbol{Q}}^{\,n+1} \cdot \hat{\boldsymbol{n}} - \Delta\Phi\, \tilde{\boldsymbol{Q}}^{\,n+1} \cdot \hat{\boldsymbol{n}} \right) \mathrm{d}S_{\xi} \\ & + \sum_{\substack{\text{boundary}\\ \text{faces}}} \int_{f,N} \left(W^{\theta} \left(M\tilde{\boldsymbol{F}} \right)^{\theta,\star} \cdot \hat{\boldsymbol{n}} + W^{\theta,\star} \left(M\tilde{\boldsymbol{F}}^{\theta} \right) \cdot \hat{\boldsymbol{n}} - W^{\theta} \left(M\tilde{\boldsymbol{F}}^{\theta} \right) \cdot \hat{\boldsymbol{n}} \right) \mathrm{d}S_{\xi}. \end{aligned} \tag{118}$$

Introducing the numerical fluxes (56),

$$\mathrm{PBT}_N = \sum_{\substack{\text{boundary}\\ \text{faces}}} \int_{f,N} \left(\Phi^{n+1} - \Phi^{n} \right) \beta \, \mathrm{d}S = \sum_{\substack{\text{boundary}\\ \text{faces}}} \int_{f,N} \left(G\left(\Phi^{n+1}\right) - G\left(\Phi^{n}\right) \right) \mathrm{d}S, \tag{119}$$

we transform (115) to

$$\begin{aligned} \mathcal{F}_v^{n+1,N} - \mathcal{F}_v^{n,N} - & \int_{\partial e \bigcup \partial\Omega,N} \left(G(\Phi^{n+1}) - G(\Phi^{n}) \right) \mathrm{d}S = \mathcal{F}^{n+1,N} - \mathcal{F}^{n,N} \\ & = -\Delta t \sum_{e} \left\langle \mathcal{J}\vec{F}^{\theta}, M\vec{F}^{\theta} \right\rangle_{E,N} + \sum_{e} \mathrm{diss}_{\mathrm{IMEX}}^{E,N}. \end{aligned} \tag{120}$$

The last step is to sum over all time steps $n = 0, \ldots, T-1$,

$$\begin{aligned} \mathcal{F}^{T,N} - \mathcal{F}^{0,N} &= -\Delta t \sum_{e,n} \left\langle \mathcal{J}\vec{F}^{\theta}, M\vec{F}^{\theta} \right\rangle_{E,N} + \sum_{e,n} \mathrm{diss}_{\mathrm{IMEX}}^{E,N} - \Delta t \sum_{\substack{\text{interior}\\ \text{faces}}} \int_{f,N} \sigma M \left[\!\left[W^{\theta} \right]\!\right]^2 \mathrm{d}S \\ &\leqslant -\Delta t \sum_{e,n} \left\langle \mathcal{J}\vec{F}^{\theta}, M\vec{F}^{\theta} \right\rangle_{E,N}, \end{aligned} \tag{121}$$

which shows that the discrete free–energy is bounded by its initial value

$$\mathcal{F}^{T,N} \leqslant \mathcal{F}^{0,N} - \Delta t \sum_{E,n} \left\langle \mathcal{J}\vec{F}^{\theta}, M\vec{F}^{\theta} \right\rangle_{E,N} \leqslant \mathcal{F}^{0,N}, \tag{122}$$

and thus, the scheme (90) is stable and satisfies a free–energy bound consistent with the continuous equation (21). Furthermore, spatial under–resolution introduces numerical dissipation proportional to interface jumps in chemical potential, $\sigma \left[\!\left[W^{\theta} \right]\!\right]^2$, and temporal under–resolution adds dissipation proportional to $\Delta\Phi^2$ and $\Delta\vec{Q}^{\,2}$. Eq. (122) assumes that $\langle \mathcal{J}\Pi, 1 \rangle \geqslant 0$. We do not provide here a proof of positivity beyond the sufficient condition given in Fig. 1. In practice we have not seen any violation of the positivity in all the numerical experiments presented herein when $S_0 \geqslant 1$.

5. Numerical experiments

In this section we show numerical experiments to address the capabilities and robustness of the fully discrete approximation. First, we perform a convergence study using the method of manufactured solutions. The experiment performed here is two dimensional in a Cartesian mesh with straight sides. Second, we compare our results with two–dimensional results available in the literature, using a Cartesian mesh, a distorted mesh, a distorted mesh with curvilinear faces, and a fully unstructured mesh forming a "T" domain. Lastly, we explore the spinodal–decomposition in a three dimensional cylindrical geometry.

5.1. Convergence study

We now address the convergence of the fully discrete scheme. To do so, we follow [26] and consider a two–dimensional unit square, $[-1,1]^2$, and impose the solution:

$$\phi_0(x,y,t) = \cos(\pi\alpha x)\cos(\pi\alpha y)\cos(t)\,. \tag{123}$$

For (123) to be solution of (1), we add a source term to the latter,

$$\frac{\phi_0}{\partial t} = \nabla\cdot\left(M\nabla\left(\frac{\mathrm{d}\Psi(\phi_0)}{\mathrm{d}\phi} - k\nabla\phi_0^2\right)\right) + q(\vec{x},t), \tag{124}$$

whose expression is,

$$\begin{aligned} q(x,y,t) = \quad & 2M\pi^4\alpha^4 k\cos(t)\cos(\pi\alpha x)\cos(\pi\alpha y) \\ & + 3M\pi^2\alpha^2\cos(t)^3\cos(\pi\alpha x)^3\cos(\pi\alpha y)^3 \\ & - 6M\pi^2\alpha^2\cos(t)^3\cos(\pi\alpha x)\cos(\pi\alpha y)^3\sin(\pi\alpha x)^2 \\ & - M\pi^2\alpha^2\cos(t)\cos(\pi\alpha x)\cos(\pi\alpha y) \\ & + 2M\pi^4\alpha^4 k\cos(t)\cos(\pi\alpha x)\cos(\pi\alpha y) \\ & + 3M\pi^2\alpha^2\cos(t)^3\cos(\pi\alpha x)^3\cos(\pi\alpha y)^3 \\ & - 6M\pi^2\alpha^2\cos(t)^3\cos(\pi\alpha x)^3\cos(\pi\alpha y)\sin(\pi\alpha y)^2 \\ & - M\pi^2\alpha^2\cos(t)\cos(\pi\alpha x)\cos(\pi\alpha y) \\ & - \sin(t)\cos(\pi\alpha x)\cos(\pi\alpha y)\,. \end{aligned} \tag{125}$$

We solve the Cahn–Hilliard equation to a final time $t_F = 0.1$, varying the polynomial order, the element spacing, and the time step size. We check the L^2 norm of the error, defined as

$$\text{error} = \|\phi - \phi_0\|_{\mathcal{J},N} = \sqrt{\sum_e \langle \mathcal{J}(\Phi-\Phi_0),(\Phi-\Phi_0)\rangle_{E,N}}. \tag{126}$$

The physical parameters are set to $M = 1$ and $k = 0.01$, and we will vary α to analyze space under–resolved and time under–resolved solutions.

5.1.1. Polynomial order convergence study (p–refinement)

In this test the mesh is a fixed 4×4 Cartesian mesh, and the polynomial order (represented in the x–axis of the figures) ranges from $N = 3$ to $N = 8$, with three time steps $\Delta t = 10^{-3}, 5\cdot 10^{-4}$, and 10^{-4}. In all these tests we take $\alpha = 1$, so that the solution is well–resolved in space with relatively coarse meshes. The results are shown in Fig. 2, where we performed the study for two penalty parameter coefficient values κ_σ, which was defined in (54): without stabilization ($\kappa_\sigma = 0$) in Fig. 2(a) and with stabilization ($\kappa_\sigma = 3$) in Fig. 2(b). Moreover, we use the IMEX Euler scheme with $K_0 = 1$ and $S_0 = 1$.

We find that the convergence is slower without interface stabilization ($\kappa_\sigma = 0$), and also that it is uneven. This even–odd phenomena has been also reported in [15] in the context of the compressible Euler equations, where it was tackled by adding interface stabilization. With interface stabilization (Fig. 2(b)), we find not only that the convergence is smoother, but errors are always lower. The curve shows the typical pattern of a polynomial order convergence study: on the one hand, for low polynomial orders the solution is under–resolved in space, and errors decrease exponentially with the polynomial order (linear decay in semi–logarithmic plot). In this region, errors are not affected by the time step Δt. On the other hand, for high polynomial orders, the solution is under–resolved in time, and thus it reaches a stagnation with further increase of the polynomial order. In this region, the error is controlled by the time step Δt, as the different plots in Fig. 2(b) show. We have represented in Fig. 3 the different errors obtained once the stagnation is reached to show that the scheme is first order accurate in time, as designed.

5.1.2. Mesh convergence study (h–refinement)

In this test, we increase the manufactured solution's wavenumber to $\alpha = 8$, so that we extend the region with spatial under–resolution. We vary the number of elements from a 16×16 mesh to a 64×64 mesh, and we consider four polynomial orders, from $N = 2$ to $N = 5$. The rest of the parameters remain the same as in Sec. 5.1.1, and we use the scheme with interface stabilization ($\kappa_\sigma = 3$). The time–step used is $\Delta t = 10^{-3}$ for $N = 2, 3$, and $\Delta t = 10^{-4}$ for $N = 4, 5$. The results are represented in Fig. 4, where we have drawn the theoretical convergence rates for each polynomial order

$$\|\phi - \phi_0\| \propto \Delta x^{N+1}. \tag{127}$$

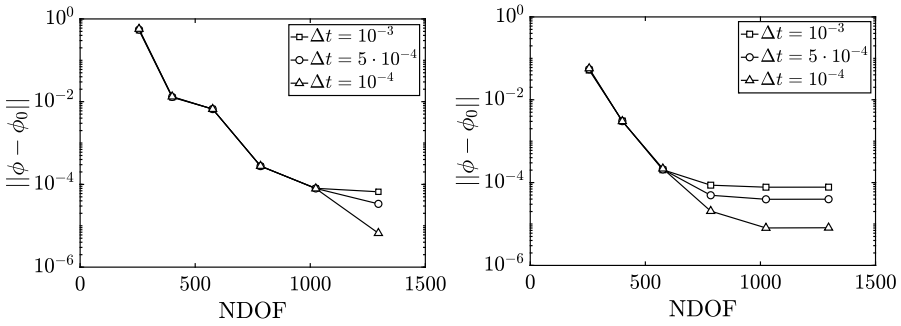

(a) Without interface stabilization ($\kappa_\sigma = 0$) (b) With interface stabilization ($\kappa_\sigma = 3$)

Fig. 2. Polynomial order convergence study without and with interface stabilization. We show that the convergence is faster and smoother with interface stabilization, and that the convergence rate is exponential only with interface stabilization.

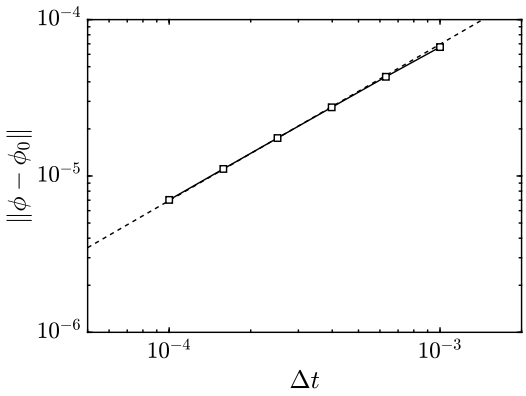

Fig. 3. Temporal convergence study. The dashed line represents the theoretical linear convergence rate. We confirm that the scheme is first order accurate in time, as designed.

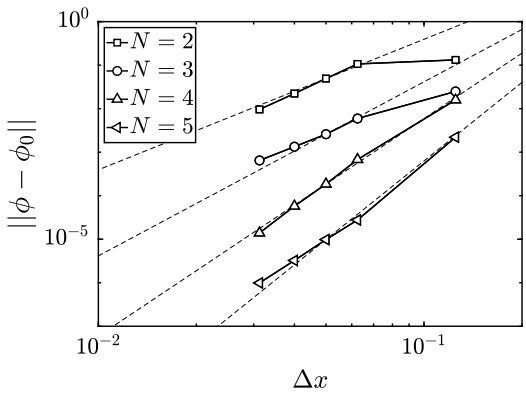

Fig. 4. Spatial convergence study for different polynomial orders. We vary the mesh spacing from $\Delta x = 0.125$ (16x16 mesh) to $\Delta x = 0.03125$ (64x64 mesh). Dashed lines represent the theoretical convergence rate, Δx^{N+1}, for each polynomial.

We find that despite adding the interface stabilization, there still remains some slight even–odd effect, as the convergence is faster than the theoretical for even polynomial orders, and slower otherwise. Similar behavior was noted in [27] and the reason behind this effect in this particular scheme still remains an open question.

5.2. Two dimensional spinodal decomposition

In this section, we compare the scheme when solving a two dimensional spinodal decomposition. The spinodal decomposition describes the phase separation process from an initial mixed state. To trigger the separation, we use the initial condition proposed in [28],

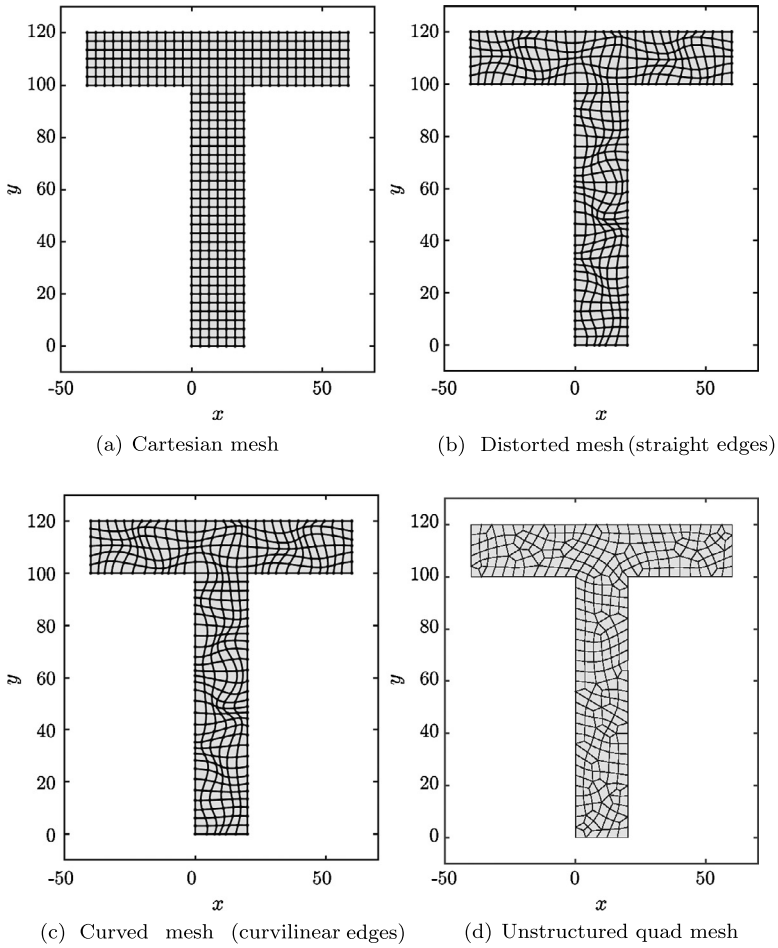

Fig. 5. Four meshes used for the spinodal decomposition test. The distorted mesh has straight faces, whilst the curved mesh edges are curvilinear.

$$\begin{aligned}\phi_0(x,y) =& 0.05\big(\cos(0.105x)\cos(0.11y) + (\cos(0.13x)\cos(0.087y))^2 \\ &+ \cos(0.025x - 0.15y)\cos(0.07x - 0.02y)\big).\end{aligned} \tag{128}$$

The domain is "T"–shaped, which we mesh using four strategies: a Cartesian mesh (Fig. 5(a)), the Cartesian mesh distorted with straight sided elements (Fig. 5(b)), the Cartesian mesh distorted with curved elements (Fig. 5(c)), and an unstructured quad mesh (Fig. 5(d)).

The parameters of the Cahn–Hilliard equation used are that of [28], but adapted to ϕ ranging from -1 to 1 (in [28] it ranges from 0.3 to 0.7),

$$M = 1.0, \quad k = 10.0, \quad \beta = 0, \quad \Delta t = 0.1, \tag{129}$$

and we use a polynomial order $N = 4$. We monitor the free–energy evolution with time and compare with the results provided in [28].

We first study the effect of the IMEX parameters K_0 and S_0 in the curved (Fig. 5(c)) and the unstructured (Fig. 5(d)) meshes. For K_0 we consider two scenarios: the Crank–Nicolson scheme, $K_0 = 1/2$, and the backward Euler scheme $K_0 = 1$. For S_0 we study three values: $S_0 = 0$, which does not guarantee stability for the non–linear terms, $S_0 = 1$, which guarantees non–linear term stability for $\Phi \in [-1, 1]$, and $S_0 = 2$, which guarantees non–linear term stability for $\Phi \in [-1.29, 1.29]$ (see Fig. 1).

The evolution of the free energy is shown in Fig. 6 for all parameter combinations and the two meshes (curvilinear in Fig. 6(a), and unstructured in Fig. 6(b)). The circles represent the reference solution from [28]. On the one hand, for the backward Euler scheme ($K_0 = 1$, solid lines in Fig. 6), there is no high impact of S_0 on the free energy. The scheme is stable even for the lowest S_0 value. Thus, the physical dissipation and the dissipation introduced by backward Euler scheme are enough to balance non–linear instabilities in this case. On the other hand, for the Crank–Nicolson scheme ($K_0 = 1/2$), the solution depends highly on S_0. For $S_0 = 0$ (represented with a dashed line), the scheme is unstable. The physical dissipation is not sufficient to counteract the instabilities that arise from the non–linear terms. For $S_0 = 1$ (solid line), we obtain

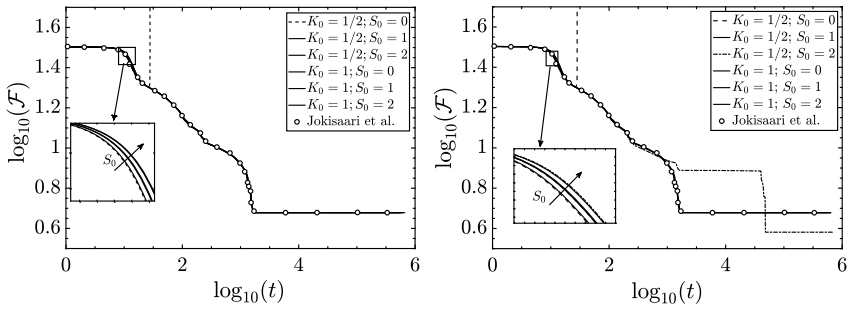

(a) Curved mesh (b) Unstructured mesh

Fig. 6. Evolution of the free–energy $\mathcal{F}$ for the "T" domain. We consider two K_0 cases: Crank–Nicolson ($K_0 = 1/2$) and backward Euler ($K_0 = 1$). We find that the solution depends on S_0 only if we use the Crank–Nicolson scheme, producing an unstable scheme if $S_0 = 0$ (dashed line), and a different solution for $S_0 = 2$ (dot–dash line in the unstructured mesh). For the rest of the cases (solid lines), the solution agrees with [28], represented with circles.

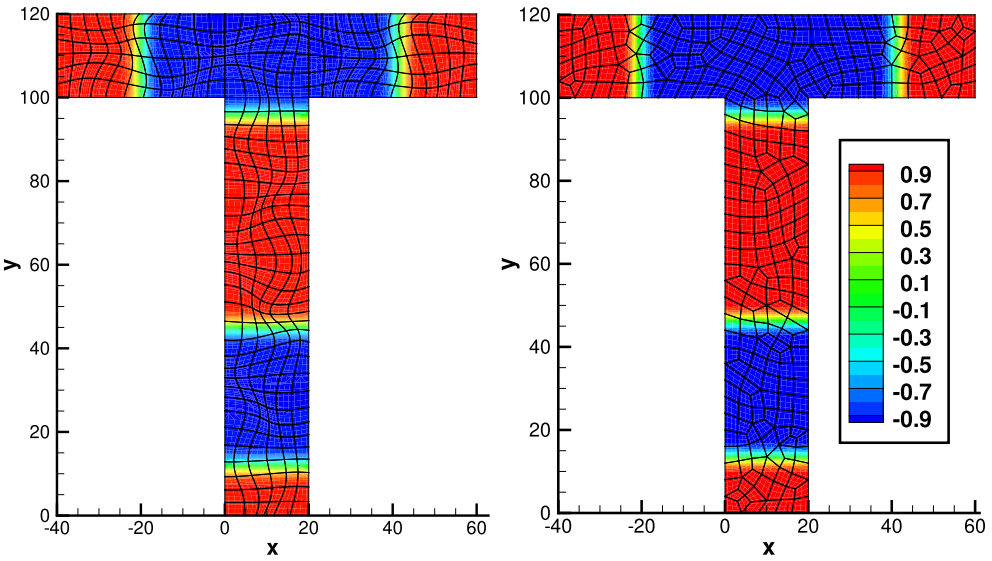

(a) Curved mesh (b) Unstructured mesh

Fig. 7. Representation of the final equilibrium solution in the curved and unstructured mesh. We find that the impact from the mesh on the solution is minimal, since interfaces are not aligned with the elements faces.

approximately the same solution as the backward Euler scheme in both meshes. However, for $S_0 = 2$ (dot–dash line), and only for the unstructured mesh, the final solution is different from the others, leading to lower free–energy values in the steady–state. Furthermore, in the detailed view (Fig. 6) we find small differences in the free–energy evolution when varying S_0. In a non–intuitive way, the free–energy decreases at a slower rate for higher S_0 values. Nonetheless, this result is still in agreement with the theoretical bound (122).

Overall, we recommend the use of the backward Euler scheme to remove the final solution dependency on S_0, and to use $S_0 = 1$ to avoid instabilities from non–linear terms, although they have not appeared in this experiment (with $K_0 = 1$).

For this scenario, we represent the differences in the free–energy evolution for the rest of the meshes considered in Fig. 5. First, in Fig. 7 we represent the final state for the curvilinear and unstructured meshes, where we find that the mesh has no visual impact on the solution, since the resulting interfaces are not aligned with the mesh.

To quantify the differences due to the mesh, we consider the Cartesian mesh (Fig. 5(a)) as the reference solution, and represent the free–energy difference of the other meshes with that. The result is represented in Fig. 8. In the y–axis we represent the difference $\log_{10}(\mathcal{F}_{\text{cartesian}}) - \log_{10}(\mathcal{F}_1)$, between the Cartesian mesh and $\mathcal{F}_1$ stands for the free–energy of the distorted (solid line), curved (dashed line) and unstructured (dash–dot line). In any case, the errors (and more substantially, in the initial and final states) remain low, and all meshes considered were stable and accurate once the IMEX parameters were set-up appropriately.

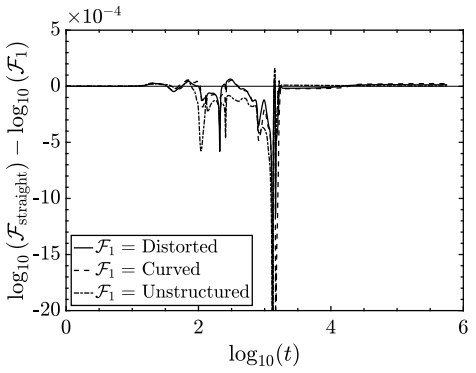

Fig. 8. Free–energy evolution comparison of the distorted (solid line), curved (dashed line), and unstructured (dash–dot line) meshes with the Cartesian mesh. We find that, despite the initial and final values being approximately the same, in the evolution the errors are maintained low (of order 10^{-3}) for the same number of degrees of freedom.

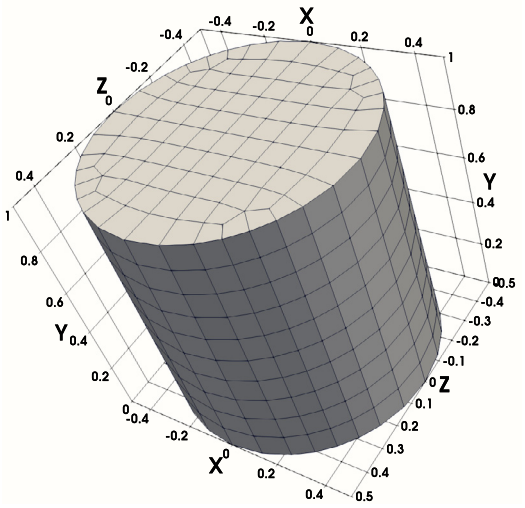

Fig. 9. Representation of the mesh used for the three dimensional spinodal decomposition simulation.

5.3. Three dimensional spinodal decomposition

We also show the solver's capability to solve the spinodal decomposition in three dimensions. We consider the interior of a cylinder ($L = D = 1$), which we divide into 920 elements. A representation of the cylinder and the mesh are provided in Fig. 9. We use order $N = 3$ polynomials, and the following values for the rest of the parameters:

$$k = 0.01, \quad M = 1.0, \quad \beta = 0, \quad \Delta t = 10^{-4}, \quad K_0 = 1, \quad S_0 = 1.0. \tag{130}$$

Initially, as in the two dimensional example, the phases are mixed, and we trigger the decomposition with the initial condition,

$$\begin{aligned} \phi_0(x, y, z) = \quad & 0.015\cos(5x - 10z)\cos(7x + 10zy + 1) \\ & + 0.02\cos(20y^2 + 15x^2)\sin(5x + 2y + 3x) \\ & + 0.02\cos(10\sqrt{y^2 + z^2})\cos(15xy)\sin(20x + 10z) \\ & + 0.01\cos(3x)\cos(3z)\cos(4y). \end{aligned} \tag{131}$$

We run the simulation until the steady–state is reached. We show the evolution of the phases in Fig. 10, where we have represented the interfaces and colored the rest with blue ($\phi = -1$) and red ($\phi = 1$). Each plot in Fig. 10 represents a different time instant, one for each power of 10. The initial condition corresponds to Fig. 10(a), and the final steady–state is Fig. 10(g). Note that the final state is achieved with a flat interface separating both phases. Additionally, in Fig. 11 we depict the evolution of the free–energy $\mathcal{F}$, showing that like in two dimensional simulations, it decreases monotonically from the initial condition to the steady state.

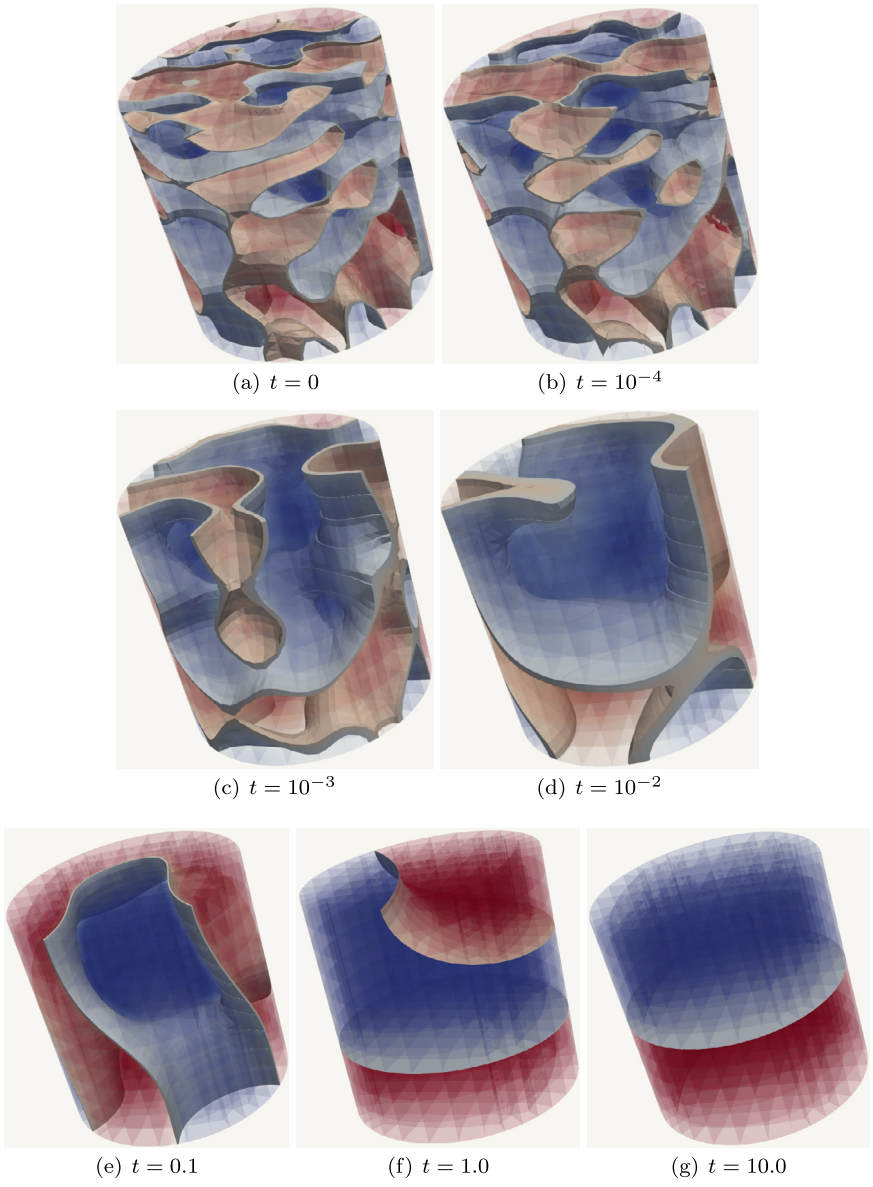

Fig. 10. Evolution of the phases with time for the three dimensional spinoidal decomposition. Blue and red contours represent the equilibrium phases $\phi = -1$ and $\phi = 1$ respectively. (For interpretation of the colors in the figure(s), the reader is referred to the web version of this article.)

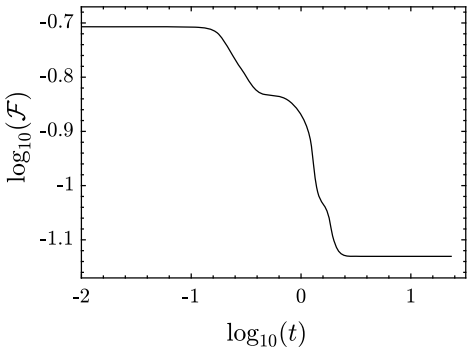

Fig. 11. Evolution of the free-energy $\mathcal{F}$ with time for the three-dimensional spinodal decomposition simulation.

6. Summary

We have developed a nodal Discontinuous Galerkin (DG) spectral element method (DGSEM) to solve the Cahn–Hilliard equation. We used the Gauss–Lobatto variant of the DG method to use the summation–by–parts simultaneous–approximation–term (SBP–SAT) property and showed that it is discretely stable. The spatial discretization uses the Bassi–Rebay 1 (BR1) method to couple inter–element fluxes, and the time discretization uses an efficient IMEX scheme. We first show the semi–discrete stability analysis (i.e. continuous in time), and later we show the fully–discrete one using the IMEX scheme. Both analyses show that the discrete free–energy is bounded in time by the initial value, which is in accordance with the continuous energy estimate. The fully–discrete stability was found to depend on a positivity condition for the phase field. Lastly, we perform a convergence study of the scheme, we compare the scheme with previous results from the literature, and perform a simulation in three–dimensional curvilinear geometries, showing that the scheme is stable (i.e. its free–energy decreases) under all conditions tested herein as proved.

Declaration of competing interest

The authors declare that they have no known competing financial interests or personal relationships that could have appeared to influence the work reported in this paper.

Acknowledgements

The authors would like to thank Dr. Gustaaf Jacobs of the San Diego State University for his hospitality. This work was supported by a grant from the Simons Foundation (#426393, David Kopriva). This work has also been partially supported by Ministerio de Economía y Competitividad under the research grant TRA2015-67679-C2-2-R. The authors acknowledge the computer resources and technical assistance provided by the Centro de Supercomputación y Visualización de Madrid (CeSViMa).

Appendix A. Stability analysis of the Crank–Nicolson scheme

It has been shown in (114) that the implicit Euler scheme used for $\vec{Q}$ in (90c) adds numerical dissipation that is proportional to the jumps in time $\Delta\vec{Q}$ squared,

$$-\frac{1}{2}k\left\langle \mathcal{J}\Delta\vec{Q}\,,\Delta\vec{Q}\right\rangle_{E,N}\leqslant 0. \tag{132}$$

This dissipation can be effectively controlled using a linear combination of $\vec{Q}^{\,n+1}$ and $\vec{Q}^{\,n}$. To show this, we define an intermediate state $\vec{Q}^{\,\theta}$,

$$\vec{Q}^{\,\theta}=K_0\vec{Q}^{\,n+1}+(1-K_0)\vec{Q}^{\,n}, \tag{133}$$

such that $K_0=1$ recovers backward Euler, $K_0=1/2$ is Crank–Nicolson, and $K_0=0$ is forward (explicit) Euler.

To study the stability, we consider (90c) and (92), where instead of $\vec{Q}^{\,n+1}$ we use $\vec{Q}^{\,\theta}$ defined in (133),

$$\langle \mathcal{J}W^{\theta},\varphi_W\rangle_{E,N}=\left\langle\left(\frac{\mathrm{d}\Psi}{\mathrm{d}\Phi}\right)^n+S_0\Phi^{n+1}-S_0\Phi^n,\mathcal{J}\varphi_W\right\rangle_{E,N}-k\int_{\partial E,N}\varphi_W\,\tilde{\boldsymbol{Q}}^{\star,\theta}\cdot\hat{\boldsymbol{n}}\,\mathrm{d}S_\xi+k\left\langle\tilde{\boldsymbol{Q}}^{\,\theta},\nabla_\xi\varphi_W\right\rangle_{E,N}, \tag{134a}$$

$$\left\langle\mathcal{J}\frac{\Delta\vec{Q}}{\Delta t},\vec{\varphi}_Q\right\rangle_{E,N}=\int_{\partial E,N}\left(\frac{\Delta\Phi^\star}{\Delta t}-\frac{\Delta\Phi}{\Delta t}\right)\tilde{\boldsymbol{\varphi}}_Q\cdot\tilde{\boldsymbol{n}}\,\mathrm{d}S_\xi+\left\langle\frac{\nabla_\xi(\Delta\Phi)}{\Delta t},\tilde{\boldsymbol{\varphi}}_Q\right\rangle_{E,N}. \tag{134b}$$

We replace $\vec{\varphi}_{\vec{Q}}=\vec{Q}^{\,\theta}$ in (134b), so that the left hand side is

$$\begin{aligned}\left\langle\mathcal{J}\Delta\vec{Q}\,,\vec{Q}^{\,\theta}\right\rangle_{E,N}&=\left\langle\mathcal{J}\left(\vec{Q}^{\,n+1}-\vec{Q}^{\,n}\right),K_0\vec{Q}^{\,n+1}+(1-K_0)\vec{Q}^{\,n},\right\rangle_{E,N}\\&=\frac{1}{2}\left\langle\mathcal{J}\vec{Q}^{\,n+1},\vec{Q}^{\,n+1}\right\rangle_{E,N}-\frac{1}{2}\left\langle\mathcal{J}\vec{Q}^{\,n},\vec{Q}^{\,n}\right\rangle_{E,N}+\left(K_0-\frac{1}{2}\right)\left\langle\mathcal{J}\Delta\vec{Q}\,,\Delta\vec{Q}\,,\right\rangle_{E,N}.\end{aligned} \tag{135}$$

When we replace $\varphi_W=\frac{\Delta\Phi}{\Delta t}$, we obtain the more general expression of (96),

$$\left\langle\mathcal{J}W^{\theta},\frac{\Delta\Phi}{\Delta t}\right\rangle_{E,N}=\left\langle\left(\frac{\mathrm{d}\Psi}{\mathrm{d}\Phi}\right)^n+S\Delta\Phi,\mathcal{J}\frac{\Delta\Phi}{\Delta t}\right\rangle_{E,N}+k\left\langle\mathcal{J}\frac{\Delta\vec{Q}}{\Delta t},\vec{Q}^{\,\theta}\right\rangle_{E,N}-k\mathrm{BT}_{E,N}\left(\frac{\Delta\Phi}{\Delta t},\vec{Q}^{\,\theta}\right). \tag{136}$$

Following the rest of the steps in the fully–discrete analysis, which remain the same, we arrive to the same bound in (122), but with new IMEX dissipation, $\mathrm{diss}_{\mathrm{IMEX}}^{\theta,E,N}$ in terms of K_0

$$\mathrm{diss}_{\mathrm{IMEX}}^{\theta,E,N} = -\left\langle \mathcal{J}\Pi, 1\right\rangle_{E,N} - \frac{1}{2}k\left(K_0 - \frac{1}{2}\right)\left\langle \mathcal{J}\Delta\vec{Q}, \Delta\vec{Q}\right\rangle_{E,N} \leqslant 0. \tag{137}$$

Thus, the amount of dissipation related to $\vec{Q}$ added by the implicit scheme varies linearly with K_0, and vanishes with $K_0 = 1/2$ (Crank–Nicolson scheme). Note that, with this approach, we cannot confirm that the explicit Euler is stable, which does not necessarily mean that it is unstable. The stability of the explicit Euler scheme is not analyzed in detail in this work as we consider it impractical due to the time step limitation imposed by the fourth order spatial derivate of the Cahn-Hilliard equation. In the numerical experiments, we set K_0 to both 1 (implicit Euler) and 1/2 (Crank–Nicolson) to see whether it is enough with the dissipation provided by $-\left\langle \mathcal{J}\Pi, 1\right\rangle_{E,N}$ and the physical dissipation for the approximation to be stable.

Appendix B. Effect of interface stabilization in $\vec{Q}^\star$

We have only considered interface stabilization in the chemical potential gradient weak form, $\vec{\mathcal{F}}^\star$. We have not considered interface stabilization in the phase field gradient, $\vec{Q}$, since we have found that it pollutes the free–energy $\mathcal{F}$. In this Appendix we show the effect of adding interface stabilization also to $\vec{Q}^\star$,

$$\vec{Q}^\star = \{\!\{ Q \}\!\} - \sigma_q \left[\!\left[\Phi \right]\!\right], \tag{138}$$

where σ_q is a positive penalty parameter. When studying the boundary terms generated by (138),

$$\mathrm{BT}_{E,N}\left(\frac{\Delta\Phi}{\Delta t}, \vec{Q}^{\,n+1}\right) = -\sigma_q \int_{\partial e,N} \left[\!\left[\Phi^{n+1} \right]\!\right] \left[\!\left[\Delta\Phi \right]\!\right] \mathrm{d}S, \tag{139}$$

we find that (139) cannot be bounded. By rearranging,

$$-\sigma \int_{\partial e,N} \left[\!\left[\Phi^{n+1} \right]\!\right] \left[\!\left[\Delta\Phi \right]\!\right] \mathrm{d}S = -\frac{\sigma_q}{2}\int_{\partial e,N} \left[\!\left[\Phi^{n+1} \right]\!\right]^2 \mathrm{d}S + \frac{\sigma_q}{2}\int_{\partial e,N} \left[\!\left[\Phi^{n} \right]\!\right]^2 \mathrm{d}S - \frac{\sigma_q}{2}\int_{\partial e,N} \left[\!\left[\Phi^{n+1} - \Phi^n \right]\!\right]^2 \mathrm{d}S, \tag{140}$$

we can see that by modifying the free–energy $\mathcal{F}$ to

$$\mathcal{F}^\sigma = \mathcal{F} + \frac{\sigma_q}{2}\sum_{\substack{\text{interior}\\ \text{faces}}}\int_{f,N} \left[\!\left[\Phi^{n+1} \right]\!\right]^2 \mathrm{d}S, \tag{141}$$

then the dissipation is bounded and equal to

$$\mathrm{diss}_\sigma = -\frac{\sigma_q}{2}\sum_{\substack{\text{interior}\\ \text{faces}}}\int_{f,N} \left[\!\left[\Phi^{n+1} - \Phi^n \right]\!\right]^2 \mathrm{d}S. \tag{142}$$

Although the interface penalization contribution is always positive, and therefore the free–energy $\mathcal{F}$ is bounded in time, we cannot confirm that the free–energy is strictly monotonic in time. In most practical cases it is, and other methods that rely on this stabilization (e.g. the interior penalty method [29]) have been found by us to work well in practice with the Cahn–Hilliard equation.

Appendix C. Supplementary material

Supplementary material related to this article can be found online at https://doi.org/10.1016/j.jcp.2019.109072.

References

[1] J.W. Cahn, J.E. Hilliard, Free energy of a nonuniform system. I. Interfacial free energy, J. Chem. Phys. 28 (2) (1958) 258–267.
[2] S. Allen, J. Cahn, Ground state structures in ordered binary alloys with second neighbor interactions, Acta Metall. 20 (3) (1972) 423–433.
[3] D. Lee, J. Kim, Comparison study of the conservative Allen–Cahn and the Cahn–Hilliard equations, Math. Comput. Simul. 119 (2016) 35–56.
[4] Y. Xia, Y. Xu, C.-W. Shu, Local discontinuous Galerkin methods for the Cahn–Hilliard type equations, J. Comput. Phys. 227 (1) (2007) 472–491.
[5] T.C. Fisher, M.H. Carpenter, High-order entropy stable finite difference schemes for nonlinear conservation laws: finite domains, J. Comput. Phys. 252 (2013) 518–557.
[6] M.H. Carpenter, T.C. Fisher, E.J. Nielsen, S.H. Frankel, Entropy stable spectral collocation schemes for the Navier–Stokes equations: discontinuous interfaces, SIAM J. Sci. Comput. 36 (5) (2014) B835–B867.
[7] W. Chen, C. Wang, X. Wang, S.M. Wise, Positivity-preserving, energy stable numerical schemes for the Cahn-Hilliard equation with logarithmic potential, J. Comput. Phys. X 3 (2019) 100031.
[8] D.A. Kopriva, A Polynomial Spectral Calculus for Analysis of DG Spectral Element Methods, Springer International Publishing, Cham, 2017, pp. 21–40.
[9] J. Chan, D.C. Fernandez, M.H. Carpenter, Efficient entropy stable Gauss collocation methods, arXiv preprint, arXiv:1809.01178.
[10] D.A. Kopriva, G.J. Gassner, An energy stable discontinuous Galerkin spectral element discretization for variable coefficient advection problems, SIAM J. Sci. Comput. 36 (4) (2014) A2076–A2099.

[11] J. Manzanero, G. Rubio, E. Ferrer, E. Valero, D.A. Kopriva, Insights on aliasing driven instabilities for advection equations with application to Gauss-Lobatto discontinuous Galerkin methods, J. Sci. Comput. 75 (3) (2018) 1262–1281.
[12] G.J. Gassner, A skew-symmetric discontinuous Galerkin spectral element discretization and its relation to SBP-SAT finite difference methods, SIAM J. Sci. Comput. 35 (3) (2013) 1233–1256.
[13] G.J. Gassner, A.R. Winters, F.J. Hinderlang, D.A. Kopriva, The BR1 scheme is stable for the compressible Navier–Stokes equations, J. Sci. Comput. 77 (1) (2018) 154–200.
[14] G.J. Gassner, A.R. Winters, D.A. Kopriva, A well balanced and entropy conservative discontinuous Galerkin spectral element method for the shallow water equations, Appl. Comput. Math. 272 (2016) 291–308, recent Advances in Numerical Methods for Hyperbolic Partial Differential Equations.
[15] G.J. Gassner, A.R. Winters, D.A. Kopriva, Split form nodal discontinuous Galerkin schemes with summation-by-parts property for the compressible Euler equations, J. Comput. Phys. 327 (Suppl. C) (2016) 39–66.
[16] J. Manzanero, G. Rubio, D.A. Kopriva, E. Ferrer, E. Valero, Entropy-stable discontinuous Galerkin approximation with summation-by-parts property for the incompressible Navier-Stokes equations with variable density and artificial compressibility, arXiv preprint, arXiv:1907.05976.
[17] A.R. Winters, G.J. Gassner, Affordable, entropy conserving and entropy stable flux functions for the ideal MHD equations, J. Comput. Phys. 304 (2016) 72–108.
[18] S. Dong, Multiphase flows of N immiscible incompressible fluids: a reduction-consistent and thermodynamically-consistent formulation and associated algorithm, J. Comput. Phys. 361 (2018) 1–49.
[19] S. Dong, An outflow boundary condition and algorithm for incompressible two-phase flows with phase field approach, J. Comput. Phys. 266 (2014) 47–73.
[20] Z. Yang, L. Lin, S. Dong, A family of second-order energy-stable schemes for Cahn–Hilliard type equations, J. Comput. Phys. 383 (2019) 24–54.
[21] A. Debussche, L. Dettori, On the Cahn-Hilliard equation with a logarithmic free energy, Nonlinear Anal. 24 (10) (1995) 1491–1514.
[22] D.A. Kopriva, Implementing Spectral Methods for Partial Differential Equations, Springer, Netherlands, 2009.
[23] D.A. Kopriva, Metric identities and the discontinuous spectral element method on curvilinear meshes, J. Sci. Comput. 26 (3) (2006) 301.
[24] F. Bassi, S. Rebay, A high-order accurate discontinuous finite element method for the numerical solution of the compressible Navier–Stokes equations, J. Comput. Phys. 131 (2) (1997) 267–279.
[25] J. Manzanero, A.M. Rueda–Ramírez, G. Rubio, E. Ferrer, The Bassi Rebay 1 scheme is a special case of the symmetric interior penalty formulation for discontinuous Galerkin discretisations with Gauss–Lobatto points, J. Comput. Phys. 363 (2018) 1–10.
[26] M. Kästner, P. Metsch, R. de Borst, Isogeometric analysis of the Cahn–Hilliard equation – a convergence study, J. Comput. Phys. 305 (2016) 360–371.
[27] M. Ainsworth, Dispersive and dissipative behaviour of high order discontinuous Galerkin finite element methods, J. Comput. Phys. 198 (1) (2004) 106–130.
[28] A. Jokisaari, P. Voorhees, J. Guyer, J. Warren, O. Heinonen, Benchmark problems for numerical implementations of phase field models, Comput. Mater. Sci. 126 (2017) 139–151.
[29] M.F. Wheeler, An elliptic collocation-finite element method with interior penalties, SIAM J. Numer. Anal. 15 (1) (1978) 152–161.